Brodogradnja Volume 76, Number 2 (2025) 76208

University of Zagreb
Faculty of Mechanical Engineering
and Naval Architecture

journal homepage: www.brodogradnja.fsb.hr

Brodogradnja

An International Journal of Naval Architecture and
Ocean Engineering for Research and Development

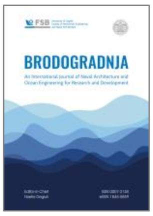

The study on dynamic modeling and path planning of a manta ray-inspired underwater glider

Yi Zhang[1], *Jianing Zhang**[1], *Zhiyang Guo*[1], *Lei Zhang*[1], *Yuchen Shang*[2], *Weimin Chen*[3]

[1] *School of Naval Architecture and Ocean Engineering, Dalian Maritime University, Dalian 116026, China*

[2] *Department of Ocean Engineering, Texas A&M University College, Station 77843, USA*

[3] *State Key Laboratory of Maritime Technology and Safety, Shanghai Ship and Shipping Research Institute Co., Ltd, Shanghai 200135, China*

ARTICLE INFO

Keywords:
Manta ray-inspired underwater vehicle
Dynamics model
Steady-state gliding state
Performance evaluation model
Path planning

ABSTRACT

This paper presents a biomimetic underwater glider inspired by the manta ray. Theoretical research is conducted to establish a dynamic model and address the path planning problem in gliding mode. A novel dynamic model for the gliding mode is developed, which takes the acceleration of a movable mass and the rate of change of a buoyancy control device as control inputs. Compared to previous methods, this model incorporates the real-time dynamic response of the control system, providing a more detailed depiction of the glider's dynamic behavior. Furthermore, the steady-state equation of gliding motion within a vertical section under ocean current conditions is derived, establishing a quantitative relationship between control states and gliding steady states, which is crucial for studying gliding motion under ocean currents. Based on the dynamic model, a performance evaluation model for the glider is proposed, with evaluation metrics including energy consumption, travel time, and detection range. The path planning problem is transformed into a multi-objective optimization problem by incorporating the performance evaluation model into the research and solved using the Non-dominated Sorting Genetic Algorithm-III (NSGA-III) algorithm for different motion strategies. Numerical results demonstrate that under both ocean current and non-current conditions, the proposed path planning method can yield path parameters that meet various performance evaluation criteria and are more comprehensive, thereby validating the effectiveness of the proposed path planning approach.

1. Introduction

In recent years, the intensification of human exploration into the enigmatic underwater world has paralleled the deepening of oceanographic research. Researchers have proposed various underwater vehicles [1-4]. As pivotal exploration carriers, unmanned Autonomous Underwater Gliders (AUGs) [5] have emerged as a focal point of research within the academic and industrial spheres. The underwater glider is regulated by

---

[*] Corresponding author.

E-mail address: zhangjianing@dlmu.edu.cn

http://dx.doi.org/10.21278/brod76208
Received 31 July 2024; Received in revised form 15 January 2025; Accepted 24 March 2025;

ISSN 0007-215X; eISSN 1845-5859

manipulating the position of a movable mass block and the overall buoyancy, thereby imbuing the vehicle with salient features such as minimal energy consumption, reduced noise levels, and streamlined motion [6]. This renders the vehicle apt for extended-duration and broad-range oceanic exploration endeavors [7,8]. A substantial array of underwater gliders, employing this mode of motion control, have been efficaciously developed and deployed. Webb*, et al.* [9] unveiled the SLOCUM, an advanced underwater glider, engineered to navigate up to 40,000 kilometers by exploiting thermal gradients for propulsion. Petritoli and Leccese [10] developed a sophisticated attitude and control system for a unique tail-fin-less autonomous underwater vehicle, distinguished by its absence of movable control surfaces. Zhou*, et al.* [11] unveiled an innovative discus-shaped underwater glider. During the underwater gliding process, the glider is subjected to gravitational forces, buoyancy, hydrodynamic forces (lift, drag, inertia), and the inertial coupling effects caused by the internal movable mass. The interaction of these forces determines the glider's motion characteristics. The external hull and internal movable masses (including battery packs, ballast, etc.) form a coupled system of multiple rigid bodies, known as a multibody motion system, which is a widely used method for constructing glider systems in research. The fluid forces acting on the body, along with the nonlinear relationship between speed and direction and the dynamic adjustment of internal mass, result in complex nonlinear motion characteristics. A typical gliding motion includes a sawtooth-like forward glide: by adjusting its buoyancy through the buoyancy control device, the glider can move up and down. During the vertical movement, the body adjusts the movable mass to change the pitch angle, generating forward velocity through the hydrodynamic forces acting on the wings. Therefore, the glider can form a sawtooth-like motion pattern in the vertical plane through the coupling of multiple forces. In addition to the sawtooth motion, the underwater glider can also perform another steady-state motion, which is a spiral trajectory underwater. By adjusting the buoyancy to make the body rise or fall while maintaining a fixed pitch angle and controlling the internal rotating mass to adjust the yaw angle, the glider can exhibit steady-state spiral motion.

With the continuous iteration and upgrading of underwater glider entities, researchers have been consistently advancing theoretical studies on underwater gliding motion[12]. Significant progress has also been made in the study of the mechanism of underwater gliding motion and dynamic models of such systems. Currently, the main methods for establishing dynamic models can be divided into two types:(1) The Newton-Euler method, based on Newton's second law and Euler's rotational equations, establishes dynamic equations by directly analyzing the forces and moments within the system. This method is suitable for rigid body systems and translational-rotational analysis, and it offers physical intuitiveness. (2) The Lagrangian method, based on the principle of least action, establishes dynamic equations by the difference between the system's kinetic and potential energy (the Lagrangian) in generalized coordinates, without directly considering forces. This method is suitable for systems with complex constraints and energy analysis.

Yang*, et al.* [13] created a dynamic model for the deep-sea glider Petrel-II using the Newton-Euler method, incorporating considerations for hull deformation at different depths and seawater density changes. Wang*, et al.* [14] established a simplified dynamical model of an underwater glider system using Lagrangian equations. Additionally, they solved the helical steady-state motion of the glider by integrating the system state equations. A method of constructing a dynamic model for underwater gliders based on Lagrangian equations, combined with an environmental compensation model, has been verified to significantly improve control accuracy [15]. Leonard and Graver [16] combined the two to derive a generalized nonlinear dynamic model, which includes the hydrodynamic force of the glider body, the glider itself and the coupling of its movable internal mass. The main difference between the two lies in the fact that the former is force-centered and physically intuitive, while the latter is energy-centered and more mathematically abstract. Zhang*, et al.* [17] proposed a recursive algorithm, noted for its rapid convergence, to solve the helical steady-state equations of the glider. Fan and Woolsey [18] proposed the nonlinear multibody dynamics model, which is designed to characterize underwater gliders operating in unstable and nonuniform flows. Zhao*, et al.* [19] applied a universal mathematical model to a specific real-world underwater glider, executing its linearization, a crucial step for the practical implementation of control methods. Liu*, et al.* [20] experimentally demonstrated a spiraling motion in underwater gliders, establishing the theoretical basis for their multimodal motion. Lyu*, et al.* [21] established a dynamic model that takes into account buoyancy and pitch control systems. Lei*, et al.* [22] merged physics-driven and data-driven modeling to introduce a novel method for underwater glider modeling, based on physics-guided neural networks.

Extensive research on the dynamic models of underwater gliders primarily aims to further parameterize the entire motion process of the vehicle, providing a foundational basis for subsequent motion control studies. To delve deeper into strategies aimed at augmenting the performance of underwater gliders, researchers have embarked on comprehensive investigations in the realms of path planning and motion strategy development. The current mainstream research approach involves describing the physical motion mechanisms of gliders through a comprehensive mathematical model [23, 24] and establishing the relationship between motion parameters and various performance metrics [25-27]. The performance metrics include energy consumption, detection range, and motion accuracy. This allows for the regulation of parameters to optimize motion strategies. This is similar to part of the content of this study. Zamuda and Hernández Sosa [28] proposed a method that applies differential evolution to underwater glider path planning. Zamuda, *et al.* [29] advanced their research by proposing a novel method for addressing constrained underwater glider path planning, significantly enhancing the glider's data collection capabilities while ensuring a controlled trajectory. Yoon and Kim [30] reformulated the trajectory optimization problem for underwater gliders into an optimal control problem, incorporating a series of intricate inequality constraints regarding depth limitations, and resolving the planning challenge. Yang, *et al.* [31] successfully enhanced the gliding range of the Petrel-L underwater glider through the strategic optimization of motion parameters tailored for diverse observation missions. Wang, *et al.* [32] employed integrated collaborative optimization and multidisciplinary optimization methods to select and refine various design parameters, thereby optimizing the motion performance of the system. To concurrently maximize both the energy utilization rate and motion speed of the glider while also improving its buoyancy positioning accuracy and energy efficiency, using established multi-objective optimization methods, the motion control parameters under gliding mode were optimized, effectively resolving the planning challenge [33, 34]. Cai, *et al.* [35] introduced a new path parameterization method and a novel velocity synthesis approach, forming a constrained optimization model for underwater glider path planning to address path planning issues of underwater gliders. Wu, *et al.* [36] developed a novel alternative model for path planning evaluation parameters and proposed a cutting-edge strategy employing the NSGA-II multi-objective optimization algorithm, successfully surmounting the complex challenge of path planning for multipoint exploration. Lan, *et al.* [37] approached the complex path planning problem of gliders navigating dense obstacles in ocean currents, via a depth-determined policy gradient method. Wang, *et al.* [38] investigated the issue of biofouling affecting the Petrel-L glider. Based on the glider's dynamic model, an internal penalty function method was used to optimize several key parameters in order to reduce the decrease in gliding range caused by biofouling. Tian, *et al.* [39] established a total energy consumption model based on the glider's dynamic model and the navigation efficiency index represented by the energy consumption per unit distance. Through mathematical derivation, the monotonicity of the total energy consumption model was proven, and an analytical solution for the globally optimal motion state with general applicability was obtained. Finally, the global optimal motion state was validated through pool experiments.

In recent research, the effects of complex ocean currents and seabed environments have been incorporated into the overall path planning problem. In [40], an energy-optimal motion planning method for gliders, which takes into account ocean currents and seabed topography, is proposed. This method, using a segmented adaptive function, achieves good results in realistic seabed topography numerical simulations. Building on this work, Hu, *et al.* [41] further analyzed the impact of motion parameters on the hybrid wing-body glider's movement. Additionally, an improved JADE optimization algorithm was proposed, combining adaptive segmentation to further enhance the glider's adaptability to the environment and reduce energy consumption. These studies effectively address the problem of multi-segment energy-optimal trajectory planning for gliders in complex seabed environments.

It is noteworthy that the majority of AUGs being developed are of the revolving body type. In comparison, a manta ray-inspired underwater vehicle offers superior load capacity, enhanced hydrodynamic efficiency, and a higher lift-drag ratio [42, 43]. Furthermore, for the study of marine biological behavior, manta ray-inspired underwater vehicles are better suited for close observation of marine life.

Summarizing the research work outlined above, the main focuses can be categorized as follows: (1)

Dynamic models of gliders were established, and optimization models based on motion parameters were derived from these dynamic models. (2) Evaluation models for glider motion, such as energy consumption, were proposed, transforming the path planning problem into a single-objective or multi-objective optimization problem. By optimizing the motion parameters, gliding paths for different requirements were determined. (3) Recent studies have considered complex ocean current conditions and seabed environments, effectively addressing multi-segment energy-optimal motion planning problems for gliders under such scenarios.

However, despite these advances, further research is required in the following areas: First, the dynamic models of gliders established in existing studies mainly use the position of the sliding mass and the buoyancy value provided by the buoyancy adjustment device as control inputs. However, it is evident that the adjustment processes of the sliding mass and buoyancy device are gradual dynamic processes, and the dynamic response of these adjustments is critical for controlling underwater gliders. Current research primarily focuses on kinematic characteristics, without fully considering the dynamic response of the system during the gliding process. Furthermore, there are significant gaps in the validation and analysis of system dynamics models under ocean current conditions within the framework of fluid dynamics. This lack of analysis reduces the accuracy of path planning and motion control under ocean current conditions. Additionally, there is insufficient research on motion strategies under varying conditions and a scarcity of studies integrating multiple performance evaluation criteria into motion planning.

To address these issues, the following work was conducted in this study: To more accurately describe the control system's response during dynamic adjustments, the sliding mass translational acceleration and buoyancy adjustment rate were used as system inputs to establish a control model. This model accounts for the adjustment processes of the control devices rather than simply defining their final states. Simultaneously, the influence of ocean currents was considered not only at the kinematic level but also by deriving the quantitative relationship between control states and steady-state gliding under ocean current conditions. This derivation is crucial for precisely controlling gliding motion under ocean currents and represents a novel contribution to glider research under such conditions. Based on the above analysis, an energy consumption model for ocean current conditions was directly established. Additionally, three evaluation criteria were proposed for gliding motion: energy consumption, time consumption, and gliding range. By integrating these criteria, the path planning problem was transformed into a multi-objective optimization problem for motion parameters, which was solved using NSGA-III. The optimization results obtained through this method can be selected based on different requirements, providing a more comprehensive solution to the path planning problem of underwater gliders.

The structure of the article is as follows. Section 1 is the nomenclature. Section 2 is the introduction. Section 3 establishes the system control model for the glider mode of the vehicle, based on movable mass-driven acceleration and the rate of change of a buoyancy control device as control inputs. Section 4 simplifies the two-dimensional sectional motion equation and analyzes the steady-state gliding under undisturbed conditions and in ocean currents. Section 5 establishes vehicle motion performance evaluation models, including models for energy consumption, time consumption, and detection range evaluation. Section 6 formulates motion strategies for exploration missions and based on the aforementioned research, proposes a method for path planning. Numerical examples are provided to demonstrate the process of the proposed method. Section 7 is the conclusion and outlook of the article.

2. Control equations of the gliding mode system

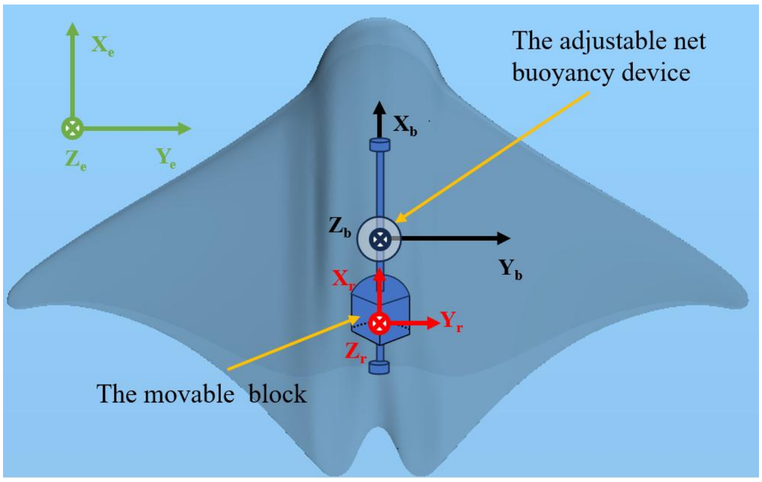

Fig. 1 The adjustment mechanism for the gliding mode of the vehicle

This study delves into the dynamics of a manta ray-inspired underwater vehicle, with a particular emphasis on exploring its gliding motion modality. The structural design of the vehicle is comprehensively illustrated in Figure 1. The vehicle incorporates a novel design where the battery pack is configured as a movable internal mass block, enhancing its manoeuvrability. Through the specific translation and rotation of this movable mass block, the vehicle's attitude can be precisely adjusted, offering superior control. Furthermore, by manipulating the state of the net buoyancy control device, the vehicle's net buoyancy can be meticulously regulated.

In this section, we derive the dynamic equations of the glider, with the entire derivation process based on the following simplifying assumptions: (1) In this study, we assume that the seawater density does not change with depth. (2) Since the range of buoyancy adjustment provided by the control device is relatively small, we approximate that the operation of the buoyancy control device does not affect the glider's centre of gravity position. (3) Due to the flexible structure of the flapping-wing configuration of the vehicle, small passive deformations may occur under actual gliding conditions. In the modelling of the pure gliding mode in this paper, we approximate that the aerofoil does not undergo deformation.

First, we define the operator $\wedge$. Taking the vector $\mathbf{a} = (\mathrm{a}_1 \quad \mathrm{a}_2 \quad \mathrm{a}_3)^{\mathrm{T}}$ as an example,

$$\overset{\wedge}{\mathbf{a}} = \begin{pmatrix} 0 & -\mathrm{a}_3 & \mathrm{a}_2 \\ \mathrm{a}_3 & 0 & -\mathrm{a}_1 \\ -\mathrm{a}_2 & \mathrm{a}_1 & 0 \end{pmatrix} \tag{1}$$

Define the vector $\mathbf{b} = (\mathrm{b}_1 \quad \mathrm{b}_2 \quad \mathrm{b}_3)^{\mathrm{T}}$. The operation $\wedge$ is defined as follows,

$$\overset{\wedge}{\mathbf{a}}\mathbf{b} = \begin{pmatrix} 0 & -\mathrm{a}_3 & \mathrm{a}_2 \\ \mathrm{a}_3 & 0 & -\mathrm{a}_1 \\ -\mathrm{a}_2 & \mathrm{a}_1 & 0 \end{pmatrix} \begin{pmatrix} \mathrm{b}_1 \\ \mathrm{b}_2 \\ \mathrm{b}_3 \end{pmatrix} = \mathbf{a} \times \mathbf{b} \tag{2}$$

For the convenience of subsequent system equation descriptions, we define the identity matrix:

$$\mathbf{c} = (\mathbf{c}_1 \quad \mathbf{c}_2 \quad \mathbf{c}_3) = \begin{pmatrix} 1 & 0 & 0 \\ 0 & 1 & 0 \\ 0 & 0 & 1 \end{pmatrix} \tag{3}$$

To delineate the system with precision, our research method defines a total of four reference frames. As illustrated in Figure 2, these frames include the inertial frame, the body frame, the local frame of the movable mass, and the flow frame, which encapsulates the dynamics of fluid forces. These reference frames are denoted as $O_e(X_e, Y_e, Z_e)$, $O_b(X_b, Y_b, Z_b)$, $O_r(X_r, Y_r, Z_r)$ and $O_f(X_f, Y_f, Z_f)$, respectively.

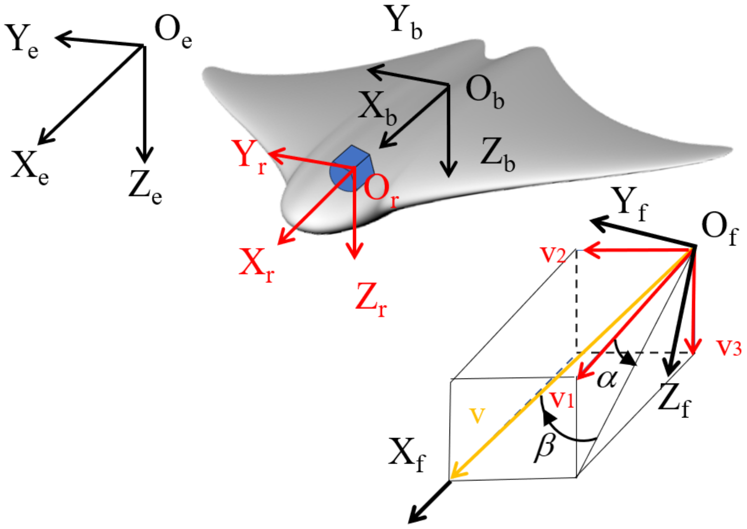

Fig. 2 The coordinate frames of underwater vehicle

Building upon the previously delineated symbol definitions, the kinematic equations governing the navigator within the inertial frame are succinctly encapsulated as follows [44].

$$\dot{\boldsymbol{V}} = \boldsymbol{R_1 v} \tag{4}$$

$$\dot{\boldsymbol{W}} = \boldsymbol{R_2 w} \tag{5}$$

where the matrices $\mathbf{R_1}$ and $\mathbf{R_2}$ denote the transformation matrices from the body coordinate system to the fixed coordinate system, with their expressions delineated as follows,

$$\boldsymbol{R_1} = \begin{pmatrix} \mathrm{C}\psi\mathrm{C}\theta & -\mathrm{S}\psi\mathrm{C}\theta + \mathrm{C}\psi\mathrm{S}\theta\mathrm{S}\phi & \mathrm{S}\phi + \mathrm{C}\psi\mathrm{C}\phi\mathrm{S}\theta \\ \mathrm{S}\psi\mathrm{C}\theta & \mathrm{C}\phi + \mathrm{S}\phi\mathrm{S}\theta\mathrm{S}\psi & -\mathrm{C}\psi\mathrm{S}\theta + \mathrm{S}\theta\mathrm{S}\psi\mathrm{C}\phi \\ -\mathrm{S}\theta & \mathrm{C}\theta\mathrm{S}\phi & \mathrm{C}\theta\mathrm{C}\phi \end{pmatrix} \tag{6}$$

$$\boldsymbol{R_2} = \begin{pmatrix} 1 & \mathrm{S}\phi\mathrm{T}\theta & \mathrm{C}\phi\mathrm{T}\theta \\ 0 & \mathrm{C}\phi & -\mathrm{S}\phi \\ 0 & \mathrm{S}\phi/\mathrm{C}\theta & \mathrm{C}\phi/\mathrm{C}\theta \end{pmatrix} \tag{7}$$

where $\mathrm{S}\theta$ represents $\sin\theta$, $\mathrm{C}\theta$ represents $\cos\theta$ and $\mathrm{T}\theta$ represents $\tan\theta$.

$\boldsymbol{R_3}$ represents the transformation matrix from the local coordinate system of the movable mass to the body coordinate system,

$$\boldsymbol{R_3} = \begin{pmatrix} 1 & 0 & 0 \\ 0 & \mathrm{C}\lambda & -\mathrm{S}\lambda \\ 0 & \mathrm{S}\lambda & \mathrm{C}\lambda \end{pmatrix} \tag{8}$$

For the purpose of articulating the fluid forces exerted on the body during motion, we establish a fluid coordinate system. The transformation matrix $\boldsymbol{R_4}$, which transitions from the flow frame to the body frame, is expressed as follows:

$$\boldsymbol{R_4} = \begin{pmatrix} \mathrm{C}\alpha\mathrm{C}\beta & -\mathrm{C}\alpha S\beta & -S\alpha \\ S\beta & \mathrm{C}\beta & 0 \\ S\alpha\mathrm{C}\beta & -S\alpha S\beta & \mathrm{C}\alpha \end{pmatrix} \tag{9}$$

In describing the forces acting on underwater moving objects, two important physical quantities are considered, one of which is the angle of attack α,

$$\alpha = \arctan(\frac{v_3}{v_1}) \tag{10}$$

The slip angle $\beta$is defined as follows,

$$\beta = \arcsin(\frac{v_2}{\sqrt{v_1^2 + v_2^2 + v_3^2}}) \tag{11}$$

With respect to the derivation of the transformation matrix, taking the transformation matrix R_1as an example, the following mathematical relationship exists:

$$\dot{\boldsymbol{R_1}} = \boldsymbol{R_1}\dot{\boldsymbol{W}} \tag{12}$$

The mass of the vehicle is divided into two parts: the movable internal mass block and the static mass (all parts except the movable internal mass block). Moreover, both parts are considered as rigid bodies, with the movable internal mass denoted as $\mathrm{m_r}$, and the static mass denoted as $\mathrm{m_s}$.

Since the range of net buoyancy adjustment is small, the shift in the center of gravity of the entire glider's static mass caused by changes in the device is considered negligible in this study [45]. The center of buoyancy provided by the device is located at the center of buoyancy of the vehicle.

In this study, we choose to characterize the dynamical behavior of the system through the formulation of momentum in classical physics. According to the definitions of the physical variables in this paper, $\boldsymbol{P_e}$ represents the linear momentum of the static mass of the body in the fixed coordinate system, and $\boldsymbol{L_e}$ represents the angular momentum of the static mass of the body in the fixed coordinate system. Based on Newton's laws of motion, the following equations can be derived,

$$\dot{\boldsymbol{P}}_{\boldsymbol{e}} = \sum_{\mathrm{k=1}}^{\mathrm{K}} \boldsymbol{F}_{\boldsymbol{e_k}} \tag{13}$$

$$\dot{\boldsymbol{L}}_{\boldsymbol{e}} = \sum_{\mathrm{k=1}}^{\mathrm{K}} (\boldsymbol{R_k} \times \boldsymbol{F}_{\boldsymbol{e_k}}) + \sum_{\mathrm{m=1}}^{\mathrm{M}} \boldsymbol{T}_{\boldsymbol{e_m}} \tag{14}$$

where $\boldsymbol{F_e}$ and $\boldsymbol{T_e}$ represent the external force and the external torque acting on the system in the inertial frame, respectively. $\boldsymbol{R_k}$ is the point of the action of hydrodynamic forces on the vehicle, which in this paper is set as the center of buoyancy, i.e., the origin of the body frame.

Within the body frame, the linear and angular momenta of the system are denoted by matrices $\boldsymbol{P_b}$ and $\boldsymbol{L_b}$, respectively. These momenta account for the additional mass and moment of inertia associated with the motion of the underwater object. In accordance with the momentum theorem, the expression for the momentum of the static mass system in the body frame is as follows,

$$\boldsymbol{P_b} = (\boldsymbol{M_s} + \boldsymbol{M_a})(\boldsymbol{v} + \boldsymbol{w} \times \boldsymbol{R_s}) \tag{15}$$

$$\boldsymbol{L_b} = (\boldsymbol{I_s} + \boldsymbol{I_a})\boldsymbol{w} + (\boldsymbol{M_s} + \boldsymbol{M_a})\boldsymbol{R_s} \times \boldsymbol{v} \tag{16}$$

where $\boldsymbol{M_s}$ is the mass matrix of the defined static mass and $\boldsymbol{I_s}$ is the inertia matrix of the static mass in the body frame.

Mapping the momentum from the body frame to the inertial frame through the transformation matrix yields the following relationship,

$$\boldsymbol{P_e} = \boldsymbol{R_1}\boldsymbol{P_b} \tag{17}$$

$$\boldsymbol{L_e} = \boldsymbol{R_1}\boldsymbol{L_b} + \boldsymbol{V} \times \boldsymbol{P_e} \tag{18}$$

Differentiating the above momentum equation yields the following formula.

$$\dot{\boldsymbol{P}}_{\boldsymbol{e}} = \boldsymbol{R_1}(\dot{\boldsymbol{P}}_{\boldsymbol{b}} + \hat{\boldsymbol{w}}\boldsymbol{P_b}) \tag{19}$$

$$\dot{\boldsymbol{L}}_{\boldsymbol{e}} = \boldsymbol{R_1}(\dot{\boldsymbol{L}}_{\boldsymbol{b}} + \hat{\boldsymbol{w}}\boldsymbol{L_b}) + \boldsymbol{R_1}\boldsymbol{v} \times \boldsymbol{P_e} + \boldsymbol{V} \times \dot{\boldsymbol{P}}_{\boldsymbol{e}} \tag{20}$$

We substitute the aforementioned expressions into the initial Equations**.** (13) and (14) which were derived based on Newton's laws, to further derive Equations (21) and (22).

$$\dot{\boldsymbol{P}}_{\boldsymbol{b}} = \boldsymbol{P_b} \times \boldsymbol{w} + \sum_{\mathrm{k=1}}^{\mathrm{K}} \boldsymbol{F}_{\boldsymbol{b_k}} \tag{21}$$

$$\dot{\boldsymbol{L}}_{\boldsymbol{b}} = \boldsymbol{L_b} \times \boldsymbol{w} + \boldsymbol{P_b} \times \boldsymbol{v} + \sum_{\mathrm{k=1}}^{\mathrm{K}} \boldsymbol{T}_{\boldsymbol{b_k}} \tag{22}$$

where $\sum_{\mathrm{k=1}}^{\mathrm{K}} F_{b_k} = R_1^T m_s g - R_1^T mg + R_4 F_f + F_{r-s}$ represents the external forces acting on the main body of the vehicle, $R_1^T m_s g$ represents the gravitational force on the static mass in the body frame, $-R_1^T mgc_3$ represents the buoyancy due to the body's displaced volume, and F_{r-s} represents the force exerted on the body by the movable mass. In the above equation, F_f represents the fluid force in the flow frame, and $\mathrm{T_f}$ represents the fluid torque in the flow frame, which can be calculated using the following method,

$$\boldsymbol{F_f} = \begin{bmatrix} -(K_{D0} + K_D\alpha^2)(v_1^2 + v_2^2 + v_3^2) \\ K_\beta(v_1^2 + v_2^2 + v_3^2) \\ -(K_{L0} + K_\alpha\alpha)(v_1^2 + v_2^2 + v_3^2) \end{bmatrix} \tag{23}$$

$$\boldsymbol{T_f} = \begin{bmatrix} (K_{MR}\beta + K_{w1}w_1)(v_1^2 + v_2^2 + v_3^2) \\ (K_{M0} + K_M\alpha + K_{w2}w_2)(v_1^2 + v_2^2 + v_3^2) \\ (K_{MY}\beta + K_{w3}w_3)(v_1^2 + v_2^2 + v_3^2) \end{bmatrix} \tag{24}$$

The hydrodynamic coefficients articulated in the aforementioned formula can be ascertained via computational fluid dynamics (CFD) and empirical methodologies.

Employing the principle of momentum, it is feasible to deduce the expressions for the absolute linear and angular momenta of the movable mass within the body frame,

$$\boldsymbol{P_{rb}} = \boldsymbol{M_r v_{rb}} \tag{25}$$

$$\boldsymbol{L_{rb}} = \boldsymbol{I_{rb} w_{rb}} \tag{26}$$

where $\boldsymbol{v_{rb}} = \boldsymbol{v} + \boldsymbol{w_r} \times \boldsymbol{R_r} + \boldsymbol{v_r}$ represents the absolute linear velocity of the slider in the body coordinate system, and $\boldsymbol{w_{rb}} = \boldsymbol{w} + \boldsymbol{w_r}$ represents the absolute angular velocity of the movable mass in the body coordinate system. $\boldsymbol{I_{rb}} = \boldsymbol{R_3 I_r R_3^T}$ represents the inertia matrix of the movable mass within the body coordinate system. Geometric relationships can be deduced as follows,

$$\boldsymbol{R_r} = \boldsymbol{x_r c_1} + \boldsymbol{r}(\sin\boldsymbol{\lambda})\boldsymbol{c_2} + \boldsymbol{r}(\cos\boldsymbol{\lambda})\boldsymbol{c_3} = (\boldsymbol{x_r} \quad \boldsymbol{y_r} \quad \boldsymbol{z_r})^{\boldsymbol{T}} \tag{27}$$

This study specifically investigates gliding motion in a vertical profile, wherein the movement of the movable slider is constrained solely to the x-axis, and considerations of rotational control are disregarded. In light of these parameters, the conditions are simplified as follows, $w_r = \lambda = 0, v_{ry} = v_{rz} = 0, w_{rb} = w$. Concurrently, given that the transformation matrix assumes the form of the identity matrix $\boldsymbol{R_3}$ in this scenario, it becomes redundant and can be disregarded, consequently leading to the equation $\boldsymbol{I_r} = \boldsymbol{I_{rb}}$.

Analogous to Equations (19) and (20), the differentiation of the absolute momentum of the slider within its local coordinate system yields the following equation,

$$\dot{\boldsymbol{P}}_{\boldsymbol{r}} = \boldsymbol{P_{rb}} \times \boldsymbol{w} + \boldsymbol{R_1^T M_r g} + \boldsymbol{F_{s-r}} \tag{28}$$

$$\dot{\boldsymbol{L}}_{\boldsymbol{r}} = \boldsymbol{L_{rb}} \times \boldsymbol{w} + \boldsymbol{P_{rb}} \times \boldsymbol{v_{rb}} + \boldsymbol{T_{s-r}} - \boldsymbol{R_r} \times \boldsymbol{F_{s-r}} \tag{29}$$

where $\boldsymbol{F_{s-r}}$ and $\boldsymbol{T_{s-r}}$ represent the force and torque exerted by the driving mechanism on the movable mass, respectively.$\boldsymbol{F_{r-s}}$ and $\boldsymbol{T_{r-s}}$ are the reaction force and torque to and $\boldsymbol{T_{s-r}}$, respectively. In accordance with Newton's Third Law of Motion, these forces are equivalent in magnitude but antithetical in direction.

Through the integration of the previously mentioned equations and the exclusion of interaction force terms, we are able to formulate the dynamic equations that govern the system.

$$\begin{aligned}(\boldsymbol{M_s} + \boldsymbol{M_a})(\dot{\boldsymbol{v}} + \dot{\boldsymbol{w}} \times \boldsymbol{R_s}) + \boldsymbol{M_r}\big(\dot{\boldsymbol{v}} + \dot{\boldsymbol{w}} \times \boldsymbol{R_r} + \boldsymbol{w} \times \dot{\boldsymbol{R}}_{\boldsymbol{r}} + \dot{\boldsymbol{v}}_{\boldsymbol{r}}\big) &= \boldsymbol{P_b} \times \boldsymbol{w} \\ &+ \boldsymbol{R_1^T M_s g} - \boldsymbol{R_1^T}(\boldsymbol{M_s} + \boldsymbol{M_r})\boldsymbol{g} + \boldsymbol{R_4 F_f} + \boldsymbol{F_{r-s}} + \boldsymbol{P_{rb}} \times \boldsymbol{w} \\ &+ \boldsymbol{R_1^T M_r g} + \boldsymbol{F_{s-r}}\end{aligned} \tag{30}$$

$$\begin{aligned}(\boldsymbol{I_s} + \boldsymbol{I_a})\dot{\boldsymbol{w}} + (\boldsymbol{M_s} + \boldsymbol{M_a})\boldsymbol{R_s} \times \dot{\boldsymbol{v}} + \boldsymbol{I_r}\dot{\boldsymbol{w}} \\ &= \boldsymbol{L_b} \times \boldsymbol{w} + \boldsymbol{P_b} \times \boldsymbol{v} + \boldsymbol{R_s M_s g} + \boldsymbol{R_4 T_f} + \boldsymbol{T_{r-s}} + \boldsymbol{L_{rb}} \times \boldsymbol{w} \\ &+ \boldsymbol{P_{rb}} \times \boldsymbol{v_{rb}} + \boldsymbol{T_{s-r}} - \boldsymbol{R_r} \times \boldsymbol{F_{s-r}}\end{aligned} \tag{31}$$

After systematic organization, the following equations are obtained,

$$\begin{aligned}(\boldsymbol{M}_s+\boldsymbol{M}_a+\boldsymbol{M}_r)\dot{\boldsymbol{v}}-(\boldsymbol{M}_s\hat{\boldsymbol{R}}_s+\boldsymbol{M}_a\hat{\boldsymbol{R}}_s+\boldsymbol{M}_r\hat{\boldsymbol{R}}_r)\dot{\boldsymbol{w}}&\\ =\hat{\boldsymbol{P}}_b\boldsymbol{w}-\boldsymbol{M}_r\dot{\boldsymbol{v}}_r+\boldsymbol{R}_4\boldsymbol{F}_f+\boldsymbol{M}_r(\boldsymbol{v}+\boldsymbol{w}\times\boldsymbol{R}_r+\boldsymbol{v}_r&\\ -\boldsymbol{w}_r\times\dot{\boldsymbol{R}}_r)\times\boldsymbol{w}&\end{aligned}\tag{32}$$

$$\begin{aligned}(\boldsymbol{I}_s+\boldsymbol{I}_a+\boldsymbol{I}_r-\boldsymbol{M}_r\hat{\boldsymbol{R}}_r\hat{\boldsymbol{R}}_r)\dot{\boldsymbol{w}}+(\boldsymbol{M}_s\hat{\boldsymbol{R}}_s+\boldsymbol{M}_a\hat{\boldsymbol{R}}_s+\boldsymbol{M}_r\hat{\boldsymbol{R}}_r)\dot{\boldsymbol{v}}&\\ =\hat{\boldsymbol{L}}_b\boldsymbol{w}+\hat{\boldsymbol{P}}_b\boldsymbol{v}+\boldsymbol{R}_s\boldsymbol{M}_s\boldsymbol{g}&\\ +\boldsymbol{R}_4\boldsymbol{T}_f+\hat{\boldsymbol{L}}_{rb}\boldsymbol{w}+\hat{\boldsymbol{P}}_{rb}\boldsymbol{v}_{rb}+\boldsymbol{M}_r\hat{\boldsymbol{R}}_r(\hat{\boldsymbol{v}}_r\boldsymbol{w}-\dot{\boldsymbol{v}}_r)+\hat{\boldsymbol{R}}_r\hat{\boldsymbol{w}}\boldsymbol{P}_{rb}&\end{aligned}\tag{33}$$

$$\dot{\boldsymbol{R}}_r=[v_{rx},0{,}0]^{\mathrm{T}}\tag{34}$$

$$\dot{\boldsymbol{v}}_r=[u(1),0{,}0]^{\mathrm{T}}\tag{35}$$

$$\dot{m}_b=u(2)\tag{36}$$

Equations (32)–(36), together with Equations (4) and (5), collectively constitute the comprehensive three-dimensional dynamic mathematical model of the entire gliding system. In traditional underwater glider control systems, the position of the movable mass is often directly used as the control input of the system, neglecting the dynamic process of the control drive. This can result in the system's inability to adapt in real-time to dynamic behaviors, leading to imprecise control. We use the driving acceleration of the movable mass and the rate of change of the net buoyancy adjustment device as the inputs for the entire control system. This state-space representation can enhance control precision: acceleration control typically allows for more precise control of the system's dynamic behavior, especially in scenarios requiring rapid response. It can more accurately describe the motion state of the system, providing superior dynamic control. This work provides a more intuitive, easily analyzable, and implementable mathematical model for the subsequent research process.

3. Vertical profile gliding steady-state analysis

In Section 2, an exhaustive derivation of the system's state response equations is conducted, considering control inputs within a three-dimensional motion context, culminating in the establishment of a comprehensive system control model. To advance the understanding of a vehicle's motion dynamics in gliding modalities, an in-depth investigation and analysis of the steady-state gliding motion within the vertical profile is imperative. The forthcoming analysis will focus on assessing the effects of ocean current disturbances on the vehicle's gliding mode.

3.1 Simplification of the equations of motion in the vertical profile

To establish the mathematical relationship between the steady-state motion parameters and control parameters, we simplify the entire three-dimensional motion equation. In the gliding motion within the vertical profile ($X_e - Z_e$ plane), the motion components within the horizontal plane do not need to be considered, thus the state space can be simplified as:

$$\boldsymbol{R_1} = \begin{bmatrix} \cos\theta & 0 & \sin\theta \\ 0 & 1 & 0 \\ -\sin\theta & 0 & \cos\theta \end{bmatrix} \boldsymbol{V} = \begin{bmatrix} x \\ 0 \\ z \end{bmatrix} \boldsymbol{W} = \begin{bmatrix} 0 \\ \theta \\ 0 \end{bmatrix} \boldsymbol{v} = \begin{bmatrix} v_1 \\ 0 \\ v_3 \end{bmatrix} \boldsymbol{w} = \begin{bmatrix} 0 \\ w_2 \\ 0 \end{bmatrix}$$
$$\boldsymbol{R_r} = \begin{bmatrix} x_r \\ 0 \\ z_r \end{bmatrix} \boldsymbol{u} = \begin{bmatrix} \dot{v}_{rx} \\ \dot{m}_b \end{bmatrix} \tag{37}$$

In the gliding motion within the vertical profile, the control of the movable slider can only slide in the X_b-axis and cannot rotate for adjustment, therefore the position of the center of mass of the movable mass changes only in the X_b-axis. By substituting the simplified state variables into the Equations (4), (5), (32) and (33), the final simplified two-dimensional pitch motion equation for the vertical section is derived [16].

$$\dot{x} = v_1 \cos\theta + v_3 \sin\theta \tag{38}$$

$$\dot{z} = -v_1 \sin\theta + v_3 \cos\theta \tag{39}$$

$$\dot{\theta} = w_2 \tag{40}$$

$$\dot{v_1} = \frac{1}{M_n(1,1)}(M_n(3,3)v_3\theta - P_{rz}\theta - m_b g \sin\theta + F_f(3)\sin\alpha - F_f(1)\cos\alpha - \dot{v}_{rx}) \tag{41}$$

$$\dot{v_3} = \frac{1}{M_n(3,3)}(M_n(1,1)v_1\theta + P_{rx}\theta + m_b g \cos\theta - F_f(3)\cos\alpha - F_f(1)\sin\alpha) \tag{42}$$

$$\begin{aligned} \dot{w}_2 = \frac{1}{I_n(2,2)}((M_n(3,3) - M_n(1,1))v_1v_3 - m_h g(-x_h\cos\theta - z_h\sin\theta) \\ +m_r g(-x_r\cos\theta - r\sin\theta) + T_f(2) - r\dot{v}_{rx}) \end{aligned} \tag{43}$$

For convenience of expression, we denote the nominal inertial mass and the nominal inertia matrix of the entire static system as: $M_n = M_s + M_a$, and $I_n = I_s + I_a$. By ignoring the behavior of the movable mass in the Y_e direction and eliminating the state variables of the body in the Y_e direction, the entire control process is simplified, facilitating subsequent solutions.

After the drive device has ceased operation, the vehicle achieves a steady-state. In this state, both the control device's configuration (encompassing the position of the movable mass and the net buoyancy adjustment device) and the vehicle's motion status remain constant. Consequently, the control device's state can be determined by resolving the equations governing steady-state gliding.

Given that both the acceleration within the system's state space and the momentum of the control device are equal to zero, this enables further simplification of the dynamic equations, specifically Equations (41) (42) and (43).

$$0 = -m_b g \sin\theta + F_f(3)\sin\alpha - F_f(1)\cos\alpha \tag{44}$$

$$0 = m_b g \cos\theta - F_f(3)\cos\alpha - F_f(1)\sin\alpha \tag{45}$$

$$\begin{aligned} 0 = (M_n(3,3) - M_n(1,1))v_1 v_3 - m_h g(-x_h \cos\theta - z_h \sin\theta + m_r g(-x_r \cos\theta \\ - r\sin\theta) + T_f(2) \end{aligned} \tag{46}$$

3.2 Steady-state motion solution under no current conditions

The system's state equations are complicated by the inclusion of two angular variables. The complexity arises because the equations are framed in a fixed coordinate system, whereas the hydrodynamic forces are initially computed in the fluid coordinate system, subsequently transformed to the body coordinate system, and ultimately retransformed to the fixed coordinate system. This sequential transformation process leads to redundant angular descriptions in the equations. To address this complexity, we introduce the kinematic relationships, depicted in Figure 3.

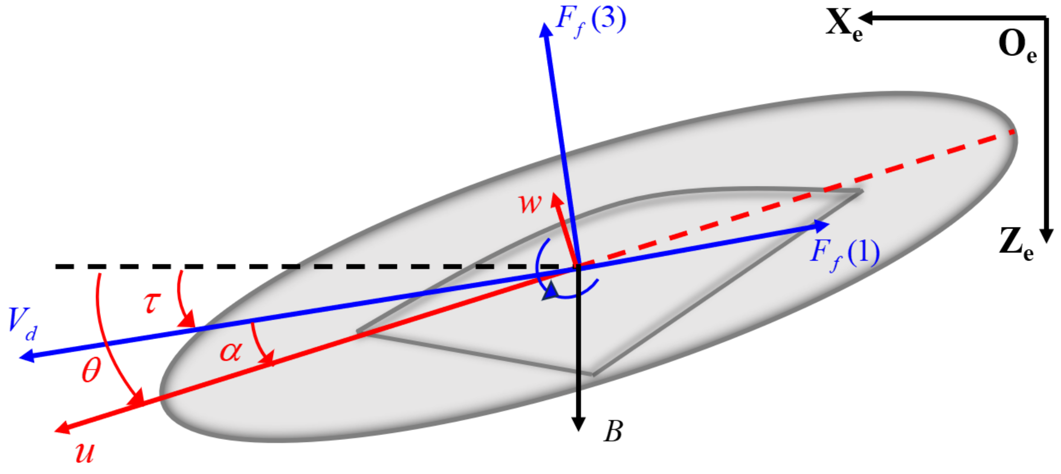

Fig. 3 Motion analysis schematic in steady-state gliding mode

The motion parameters for steady-state gliding in the vertical plane include the angle τ of the trajectory with respect to the X_e direction, the glide speed V, and the angle of attack α of the vehicle, which describes its attitude. The parameters for steady-state motion control include the position x_r of the movable mass on the body frame, and the mass m_b of the net buoyancy adjustment device.

The steady-state forces in the flow frame are directly related to those in the inertial frame through the new angular definition τ,

$$\tau = \theta - \alpha \tag{47}$$

By using the angle τ, the complex handling of θ and α can be bypassed directly. The net buoyancy in the above steady-state equations can be described in the inertial frame through a new transformation matrix as follows,

$$\begin{bmatrix} 0 \\ B \end{bmatrix} = \begin{bmatrix} \cos\tau & \sin\tau \\ -\sin\tau & \cos\tau \end{bmatrix} \begin{bmatrix} K_{D0} + K_D \alpha^2 \\ K_{L0} + K_L \alpha \end{bmatrix} V^2 \tag{48}$$

Under normal operating conditions, the gliding speed is $V \neq 0$, and the angle of the glide path is $\tau \neq \pm\frac{\pi}{2}$. Therefore, when $V = V_d$ and $\tau = \tau_d$ Equation (35) can be further organized into the following form,

$$\alpha_d^2 + \frac{K_L}{K_D} tan\, \tau_d\, \alpha_d + \frac{1}{K_D}(K_{D0} + K_{L0}\, tan\, \tau_d) = 0 \tag{49}$$

$$m_{bd} = \left(-\frac{\sin \tau_d\,(K_{D0} + K_D \alpha_d^2)}{g} + \cos \tau_d\,(K_{L0} + K_L \alpha_d)\right) V_d^2 \tag{50}$$

From Equation (49), the angle of attack under the set conditions can be derived. However, to ensure that the quadratic equation has solutions, the discriminant must satisfy the following condition:

$$(\frac{K_L}{K_D} \tan \tau_d)^2 - \frac{4}{K_D}(K_{D0} + K_{L0} \tan \tau_d) \geq 0 \tag{51}$$

The feasible range of τ_d should ensure that Equation (49) has real solutions, subject to the following constraints,

$$\tau_{\mathrm{d}} \in \left(\tan^{-1}\left(2\frac{K_D}{K_L}\left(\frac{K_{L0}}{K_L} + \sqrt{\left(\frac{K_{L0}}{K_L}\right)^2 + \frac{K_{D0}}{K_D}}\right), \frac{\pi}{2}\right) \cup \left(-\frac{\pi}{2}, \tan^{-1}\left(2\frac{K_D}{K_L}\left(\frac{K_{L0}}{K_L} - \sqrt{\left(\frac{K_{L0}}{K_L}\right)^2 + \frac{K_{D0}}{K_D}}\right)\right)\right)\right) \tag{52}$$

When the constraints are satisfied, the angle of attack α_d under the set conditions can be obtained using the quadratic formula as follows,

$$\alpha_{\mathrm{d}} = \frac{1}{2}\frac{K_L}{K_D} \tan \tau_{\mathrm{d}} \left(-1 + \sqrt{1 - 4\frac{K_D}{{K_L}^2} \cot \tau_d\,(K_{D0} \cot \tau_d + K_{L0})}\right) \tag{53}$$

By substituting the value of α_d into Equation (37), the state m_{bd} of the net buoyancy adjustment device can be determined,

$$\begin{aligned} x_{rd} = (m_h g(-x_h \cos\theta - z_h \sin\theta) + (M_n(3,3) - M_n(1,1)) v_1 v_3 \\ + T_f(2))/(m_r g \cos\theta) - r \tan\theta \end{aligned} \tag{54}$$

Through the resolution of the state equations, the range of angles delineating the vehicle gliding trajectory in the vertical plane has been precisely determined. Concurrently, a quantitative derivation has been made of the relationship between the states of the internal movable mass, the net buoyancy adjustment device, and the motion parameters during a steady-state glide in the absence of current.

3.3 Steady-state motion solution under current conditions

Oceanic currents significantly influence the gliding dynamics of navigational vehicles. In the context of this research, vehicle exploration missions are confined to smaller bodies of water, leading to the assumption that the intensity and direction of currents remain consistent and invariant with depth.

The current velocity V_{cx} in the X_e-axis significantly influences the glide speed, whereas the current V_{cy} in the Y_e-axis chiefly impacts the vehicle's heading. The current strength in the Z_e-axis is virtually negligible. The currents in the Y_e-axis exert minimal influence on the glide performance of torpedo-shaped underwater gliders [46]. Inspired by the manta ray, this underwater vehicle has a very small lateral surface area, comparable to that of traditional torpedo-shaped underwater gliders, thereby rendering the influence of current V_{cy} on its directional heading minimal. Moreover, the manta-ray-inspired design of this underwater vehicle encompasses a combination of high maneuverability with both gliding and flapping mechanisms. Throughout the gliding phase, real-time course corrections are achievable via feedback control systems. Consequently, for the sake of simplifying computational models, the effect of the current V_{cy} on navigation can be overlooked, focusing instead on the influence of a constant current V_{cx} on the vehicular motion strategy.

As illustrated in Figure 4, we assume a constant current velocity V_{cx} along theX_e-axis (neglecting the current velocity along the Z_e-axis). In the inertial frame, the vehicle glides at a speed V_d in a direction that forms an angle τ_d with the X_e-axis.

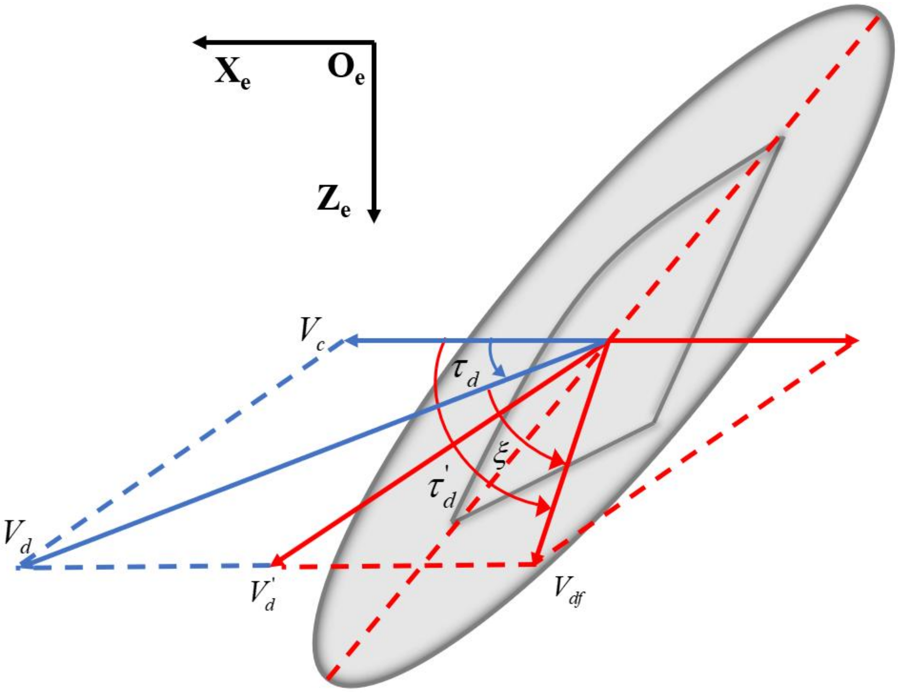

Fig. 4 Steady-state gliding motion analysis in ocean current environment

Based on geometrical knowledge, the following conclusions can be drawn.

3.3.1 When V_{cx} forms an acute angle with the direction of navigation (in a downstream state):

$$V_{df} = \sqrt{4V_{cx}^2 + V_d^2 - 4V_{cx}V_d \cos \tau_d} \tag{55}$$

Where V_{df} represents the velocity of the vehicle relative to the fluid in the flow frame, $V_d^{'}$ represents the velocity of the vehicle in the fixed frame without considering the influence of currents, which combines with the current velocity to form V_d.

$$\tau_d^{'} = \tau_d + \xi \tag{56}$$

wherein $\xi = \arccos(\frac{V_d^2 + {V_{df}}^2 - 4{V_{cx}}^2}{2V_dV_{df}})$.

3.3.2 When V_{cx} forms an obtuse angle with respect to the navigation speed (in a countercurrent state):

$$V_{df} = \sqrt{4V_c^2 + V_d^2 - 4V_c V_d \cos(\pi - \tau_d)} \tag{57}$$

$$\tau_d^{'} = \tau_d - \xi \tag{58}$$

Equation (56) still applies.

After derivation, gliding in the inertial frame at speed V_d and angle τ_d, owing to the impact of ocean currents, the actual motion parameters involved in steady-state analysis in the fluid frame become navigation speed V_{df} and angle $\tau_d^{'}$. By substituting motion parameters V_{df} and $\tau_d^{'}$ into Equations (50), (53) and (54), we ultimately obtain the relationships between motion parameters and control parameters in ocean current environments.

4. Establishing the models for evaluating vehicle performance

The gliding motion mode of a manta ray-inspired underwater vehicle is crucial for establishing its motion performance evaluation model. This paper details the comprehensive motion adjustment process within a singular glide profile of the aforementioned vehicle.

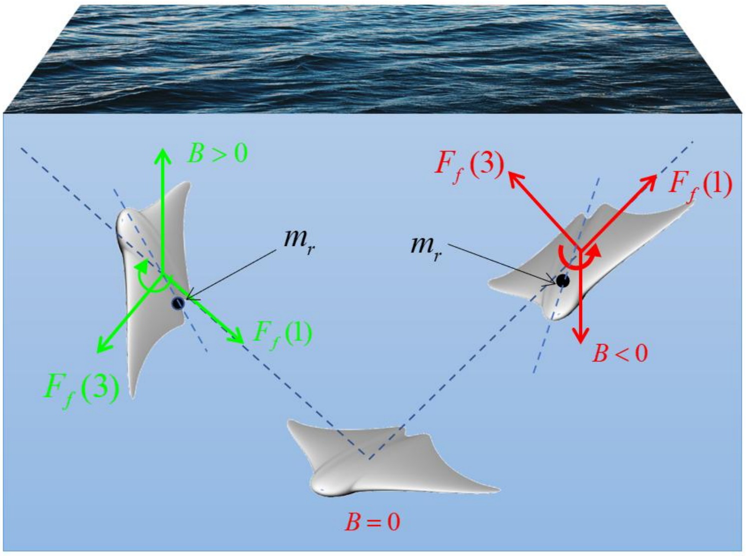

Fig. 5 Force analysis on the airframe in gliding mode

As depicted in Figure 5, initially, the vehicle maintains neutral buoyancy. Upon determining the gliding state, the drive device moves the movable slider to position x_{rd1} and adjusts the net buoyancy adjustment device to weight m_{bd1}. Upon reaching the designated depth, the control devices (slider and buoyancy chamber) return to their equilibrium positions. The control state is adjusted to m_{bd2} and x_{rd2}. Upon ascent to the preset position, it reverts to a state of neutral buoyancy. This research assumes symmetrical paths in the ascending and descending stages, thereby maintaining uniformity in velocity and angle parameters between the descent and ascent phases, denoted as $V_1 = V_2 \tau_1 = \tau_2$. This operational configuration streamlines the mathematical formulation of gliding motion, which is applicable to both individual motion cycles and extensive motion planning, thereby enhancing the efficiency of optimization calculations in the motion planning phase.

Subsequently, we utilize the transformations of motion parameters in gliding mode to develop models for energy consumption, time expenditure, and detection range assessment for the vehicle.

4.1 Energy consumption model

Throughout the vehicle gliding phase, the principal energy consumption is attributed to several key components: the buoyancy adjustment device, which encompasses the energy utilization of the pump regulating the buoyancy chamber's volume. The attitude adjustment device, involves the energy use of the motor that manipulates the movable slider's position. The control system, accounts for the operational energy expenditure of the central decision-making system. The detection system, includes the operational energy use of the assorted sensors onboard the vehicle. By utilizing the transformations of motion parameters in gliding mode, we construct models to quantify the vehicle's energy consumption, time consumption, and detection range.

The energy consumption E_1 of the buoyancy adjustment system is determined by the state of the buoyancy adjustment device during the gliding phase. Based on the motion adjustment process of a single profile, the energy consumption function for this part is as follows,

$$E_1 = \left|\frac{m_{bd1}}{\rho}\right|\left(\frac{p(D)}{q(D)}+\frac{p_v}{q_v}\right)+\left|\frac{m_{bd2}}{\rho}\right|\left(\frac{p(D)}{q(D)}+\frac{p_v}{q_v}\right) \tag{59}$$

where $p(D)$ and $q(D)$ are functions of the navigation target depth D. For fluid density ρ, we take the value $\rho = 1035 kg/m^3$. Based on [25], we select the following data for energy consumption calculation,

$$p(D) = (28.212 + 0.017841D)\ \mathrm{W} \tag{60}$$

$$q(D) = ((1.7e-6)-(1.98e-10)D)\ \mathrm{m^3/s} \tag{61}$$

4.1.1 Energy consumption of the attitude adjustment system

$$E_2 = 2\left|\frac{x_{rd1}}{v_{rx}}\right| p_r(\theta) + 2\left|\frac{x_{rd2}}{v_{rx}}\right| p_r(\theta) \tag{62}$$

where v_{rx} is the movement speed of the movable slider and $p_r(\theta)$ is the driving power of the movable slider, which varies with the pitch angle θ of the vehicle. In this paper, since the value of ξ is very small, it follows that $\theta \approx \tau$. Therefore, the following relationship exists,

$$p_r(\theta) \approx p_r(\tau) = (1.43 + 0.064|\tau|)\mathrm{W} \tag{63}$$

For the movement speed of the movable slider in the manta ray-inspired underwater vehicle studied, we take the average speed of movement during the control process to be approximately $v_{rx} = 0.1$ m/s.

4.1.2 Energy consumption of the control system

$$E_3 = \left(\frac{l_d}{|V_1 \cos\tau_1|}\right) p_c \tag{64}$$

When a current condition exists, meaning that there is a fixed v_{cx}, it leads to a change in the relative velocity in the flow frame, thereby altering the steady-state space of the glider. Below, we conduct a detailed study of the current conditions, rederive the relationship between the state variables of the control device and the state of the glider under the new steady-state, and update the expression of the energy consumption function:

$$E_3 = \left(\frac{l_d}{|V_1 \cos\tau_1 + V_{cx}|}\right) p_c \tag{65}$$

where l_d represents the designed X_e-direction travel distance for a single profile movement. p_c is the operational power of the vehicle's control system, for which the data in this study is taken as $p_c = 2W$.

4.1.3 Energy consumption of the detection system

$$E_4 = \frac{l_d}{|V_1 \cos \tau_1|} p_1 + 2\left(\frac{Dt}{t(V_1 \sin \tau_1) + d_s}\right) p_2 \tag{66}$$

Similarly, in the presence of currents:

$$E_4 = \frac{l_d}{|V_1 \cos \tau_1 + V_{cx}|} p_1 + 2\left(\frac{Dt}{t(V_1 \sin \tau_1) + d_s}\right) p_2 \tag{67}$$

where p_1 is the average power consumption of sensors during gliding conditions. p_2, t and $\mathrm{d_s}$ are the average power of the depth sensor, the duration of a single activation, and the depth sampling interval, respectively. For the manta ray-inspired underwater vehicle proposed in this paper, according to the literature [25], the relevant data in the formula are taken as the following values:$p_1 = 0.2\ W,\ p_2 = 1.92\ W,\ t = 3\ s,\ d_s = 30$ m

Ultimately, combining the energy consumption functions of the abovementioned parts, we obtain the total energy consumption function for a single profile gliding during the gliding phase of the entire vehicle,

$$E = (E_1 + E_2 + E_3 + E_4)/1000 \tag{68}$$

Equations (59) to (67) illustrate that the energy consumption of the glider's navigation will vary with changes in the control parameters m_{bd}, x_{rd} and the motion parameters V_1, τ_1.

4.2 Time consumption model

When conducting underwater detection tasks, the time consumption of the task is an important indicator for evaluating navigation performance. As the single-profile motion studied in this paper is symmetrical in the ascending and descending phases, that is $V_1 = V_2$, the total time consumption can be expressed as follows:

$$T = \frac{l_d}{|V_1 \cos \tau_1|} \tag{69}$$

From the expression of the time consumption function, it can be derived that T varies with the change in the path parameter V_1, τ_1.

4.3 Detection range evaluation model

The paramount task of underwater vehicles encompasses the detection of target aquatic environments, wherein the detection range serves as a pivotal indicator for assessing motion performance. An expanded detection range at a predetermined travel distance equates to necessitating a more profound depth in the planned path. From geometric principles, the following expression for the target depth can be derived.

$$D = l_d \tan \tau_1 \tag{70}$$

The target depth should remain within the safe depth limit $(D < D_d)$.We use the depth D of the zigzag trajectory to measure the detection range. Equation (70), indicates that D is also a function of the path parameters V_1, τ_1.

We develop comprehensive models for energy consumption, time consumption, and detection range. These models, articulated through control and motion parameters, serve to evaluate the vehicle's motion performance.

5. Path planning algorithm

When the manta ray-inspired underwater vehicle enters a gliding state, it involves not only the activation of the propulsion mechanism but also the engagement of sonar and various other detection sensors. Consequently, within the range of underwater detection, the vehicle must optimize its control parameters to align with diverse operational scene requirements, thereby charting a path that optimally balances safety and efficiency across multiple objective functions. To address various operational task requirements, the first step involves formulating a corresponding motion optimization framework.

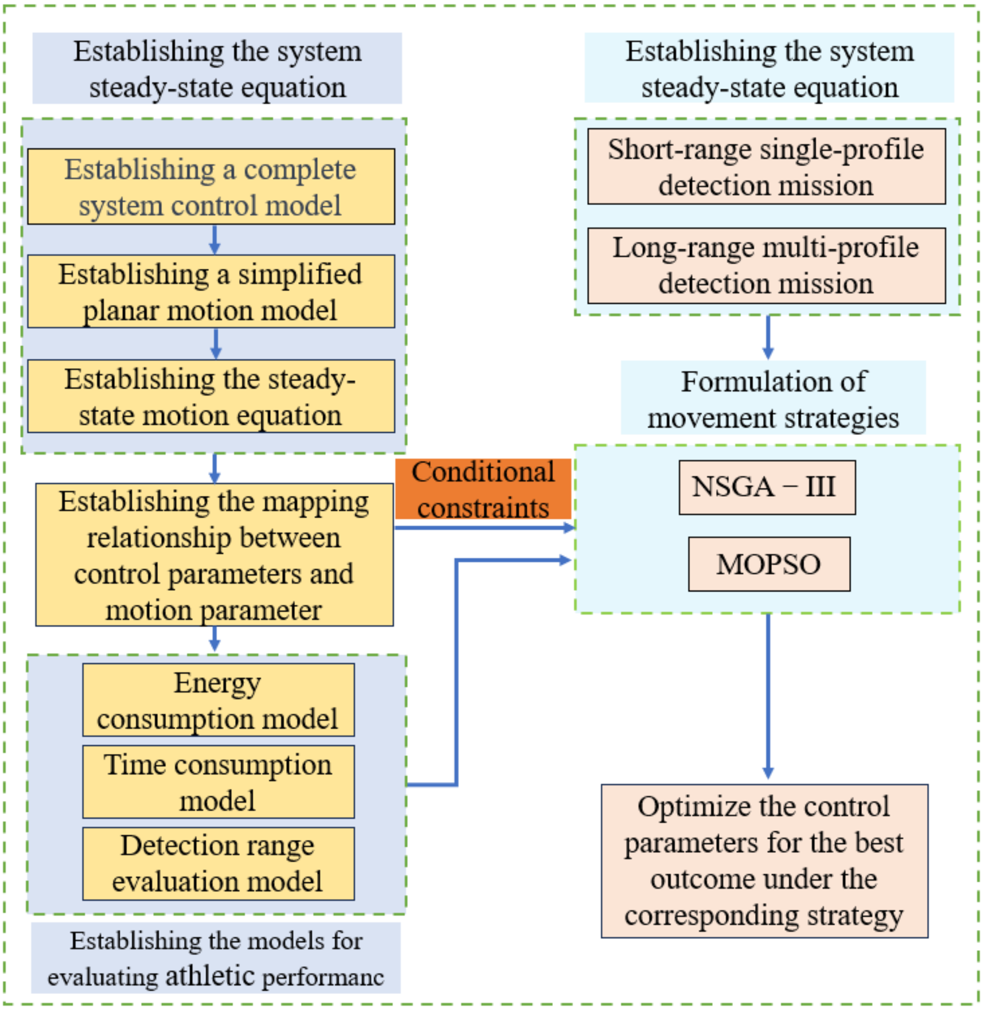

Fig. 6 Flowchart for the optimization and solution process of motion strategy

The comprehensive workflow of the path planning study is systematically illustrated in Figure 6. The computational process is segmented into three distinct phases. The initial phase involves establishing the motion model, incorporating the influence of ocean currents to derive the steady-state equation, and elucidating the interrelations among the variables. The second phase involves the construction of a motion performance evaluation model. The third phase is dedicated to formulating a motion strategy, integrating it with the evaluation model, and employing a multi-objective optimization function to refine the path planning problem.

5.1 Evaluation model for single-profile motion

The first detection mode involves near-target point single-profile detection. When addressing detection tasks in proximity to target points, frequent transitions in the gliding state can significantly escalate the energy consumption associated with the detection mission. Consequently, the vehicle is configured to utilize a single-profile gliding motion for short-distance detection tasks within unknown environments. Upon reaching the vicinity of the target point following a single planned movement, the ensuing path is reconfigured in accordance with the acquired environmental information. This particular scenario is depicted in Figure 7.

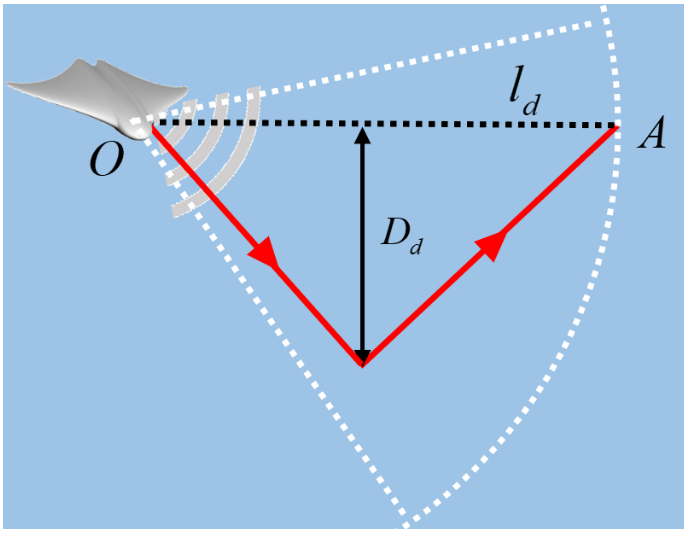

Fig. 7 Schematic of detection motion strategy for a single profile

To enhance the efficacy of diverse exploration tasks, the motion planning results of the glider should ideally combine the advantages of higher navigation speed, lower energy consumption, and a larger detection range. After setting the motion forms for the exploration tasks, we use genetic algorithms and particle swarm optimization algorithms to study the trajectory optimization problems under different motion methods. Within varying task contexts, by employing the vehicle's energy consumption, navigation speed, and detection range as objective functions, multi-objective optimization will be conducted to resolve the planning challenges, with the goal of deriving the optimal gliding strategy.

5.1.1 Without current conditions

From the derivations presented above, we establish that E, T, D is a function of the path planning parameter V, τ. To ensure the optimal performance of the glider, we determine the optimal path parameters through optimization calculations. The optimized mathematical model is presented below.

$$\begin{cases} \min E\ (V_1, \tau_1), \min T\ (V_1, \tau_1), \max D\ (V_1, \tau_1) \\ s.t. \quad V_1 \in [V_{\min}, V_{\max}], \tau_1 \in \left(-\frac{\pi}{2}, -\tau_{\min}\right) \cup \left(\tau_{\min}, \frac{\pi}{2}\right) \\ \qquad x_{rd1}, x_{rd2} \in [-0.05, 0.05], m_{bd1}, m_{bd2} \in [-1,1] \end{cases} \tag{71}$$

In the numerical simulation, calculations were predicated on the following working conditions: the target point was situated 300 m away under static water conditions. For the expediency of computation in the optimization problem-solving process, the reciprocal of the target depth D is utilized as the optimization parameter. This means that the smaller the optimization objective is, the larger the detection range that can be achieved.

Equation (71) delineates a multi-objective optimization problem, to be addressed using both the Nondominated Sorting Genetic Algorithm III (NSGA-III) and a particle swarm-based multi-objective optimization algorithm. Each algorithm employs the Pareto optimality principle as a foundational theory for solving)multi-objective optimization problems [47]. The specific parameter configuration for NSGA-III is comprehensively detailed in Table 2.

Table 2 NSGA-III multi-objective optimization computation parameters.

Population size	Number of generations	Crossover probability	Crossover index	Mutation probability	Mutation index
200	100	0.5	100	0.6	120

The parameter configuration for the particle swarm-based multi-objective optimization algorithm is given in Table 3.

Table 3 MOPSO multi-objective optimization computation parameters.

Population size	Number of iterations	Crossover probability	Crossover index	Mutation index
200	100	0.5	50	100

The parameters of the glider and its control devices used in numerical calculation were expressed in Table 4.

Table 4 Parameters of the glider's mass and control devices.

Mass	15 kg
Static hull mass	14 kg
Movable sliding block adjustment range	Translational range:-50 mm $-$ 50 mm Rotational range： $\pm\frac{\pi}{2}$ Mass： 2 kg
Buoyancy adjustment range	± 1 kg

We used the CFD method to calculate the hydrodynamic parameters of the vehicle, which were used in steady-state analysis. The specific values of the parameters obtained by fitting were expressed in Table 5.

Table 5 Calculated Values of Hydrodynamic Parameters

K_{D0}	18.36 kg/m
K_D	112.76 kg/m/rad^2
K_{L0}	-0.24 kg/m
K_α	324.10 kg/m/rad
K_{M0}	0.021 kg
K_M	-39.37 kg/rad
K_{w2}	-189.56 kg s/rad^2

To verify the convergence of the optimization calculations for path planning pertaining to short-distance detection tasks in unknown environments, we independently conduct three distinct optimization calculations employing two different methods. The optimization calculations in this study were performed using MATLAB 2023b. The computations were conducted on a computer with the following configuration: Windows 11, 64-bit, equipped with an AMD Ryzen 9 5900X 12-Core processor. The resulting Pareto frontiers are shown in Figure 8.

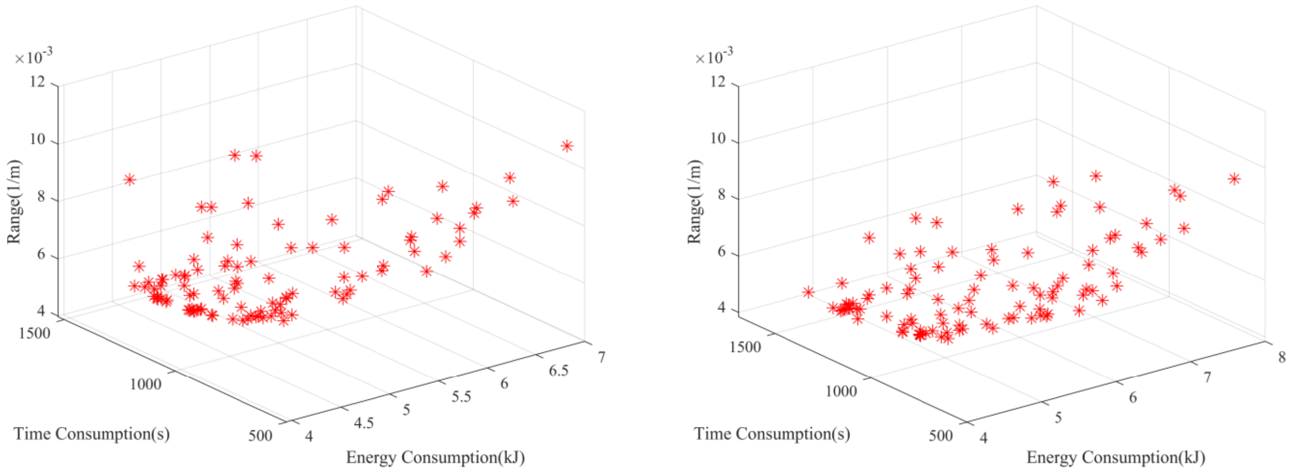

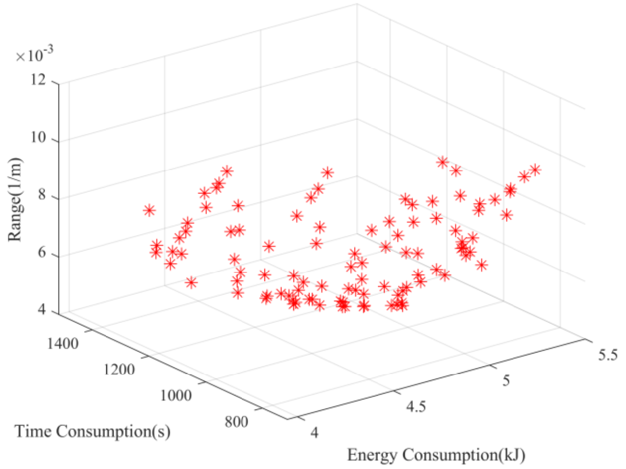

(a) NSGA-III

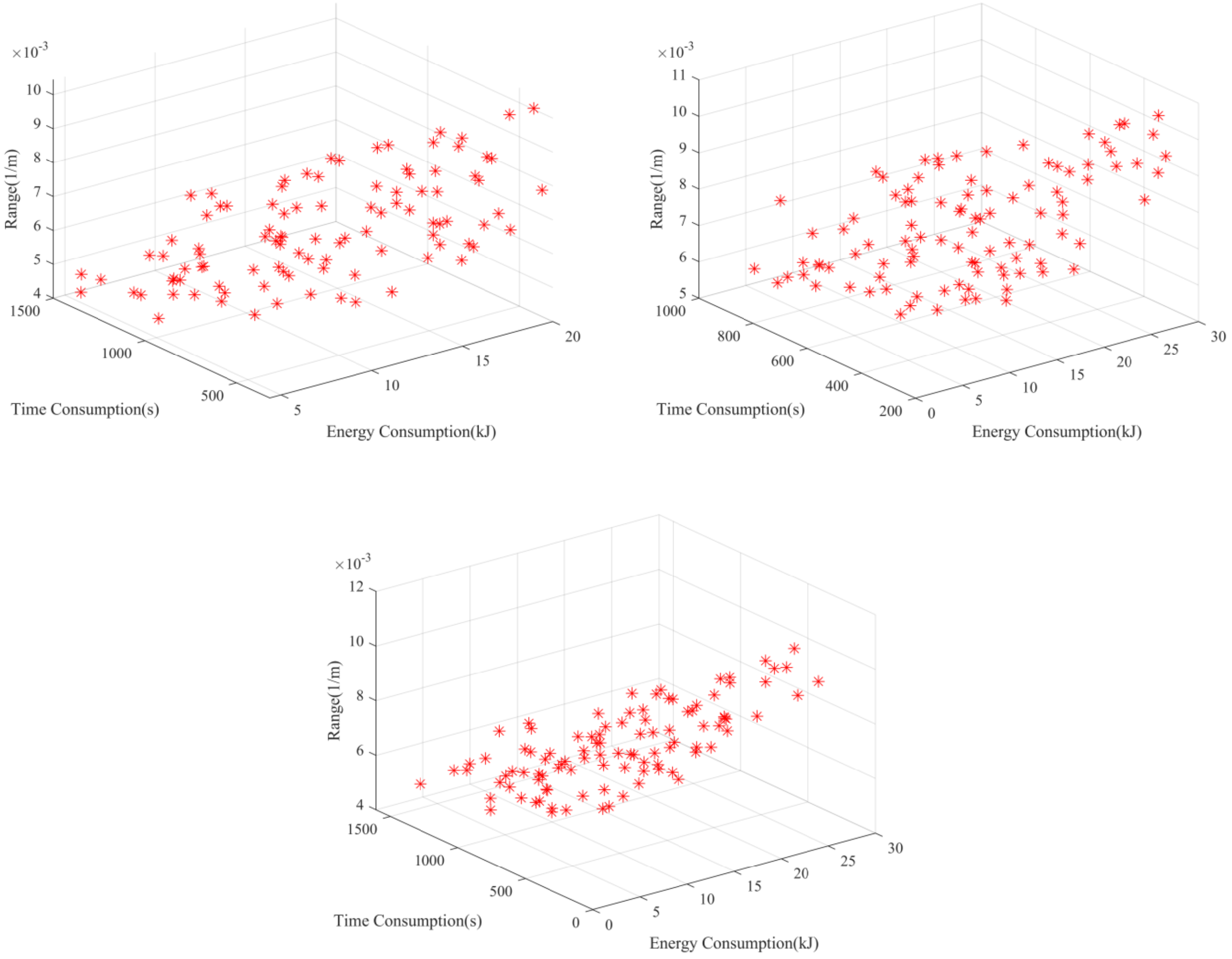

(b) MOPSO

Fig. 8 Multi-objective optimization results in Pareto frontier

As illustrated in Figure 8, we employed two solution methods for the multi-objective optimization problem: NSGA-III and MOPSO. Figure 8(a) presents the results of three independent optimization runs using NSGA-III, while Figure 8(b) shows the outcomes of three independent runs using MOPSO. The three independent computation results are 98.3256 s, 108.4352 s, and 96.7432 s for NSGA-III, and 121.6742 s, 115.8962 s, and 128.7854 s for MOPSO. For different operating conditions, multiple independent optimization runs were conducted. It is worth noting that for each operating condition in this study, multiple independent optimization computations were performed. However, only three Pareto frontier results are presented in the main text, while the remaining optimization results are provided in the appendix. And the data in Tables 2 and 3 also indicate that the NSGA-III algorithm requires lower computational costs. Analyzing the optimization results depicted in Figure 8 reveals that NSGA-III consistently generates more stable Pareto frontiers for this specific problem, demonstrating its superior suitability for addressing optimization challenges in this context.

The three independent optimization results shown in Figure 8(a) confirm the convergence of the NSGA-III algorithm. Furthermore, the Pareto frontiers in the figure visually highlight the conflicting relationships among the three optimization objective functions (energy consumption metric, time expenditure metric, and detection range metric).

Table 6 The non-dominated solution computation results.

Case	Angle (rad)	Velocity (m/s)	m_{bd1} (kg)	m_{bd2} (kg)	x_{rd1} (m)	x_{rd2} (m)	Energy (kJ)	Time (s)	Area (1/m)
1	±0.7029	0.3545	-0.122	0.126	0.032	-0.031	4.02	1109	0.0078
2	±0.5598	1.50	-0.878	0.885	0.014	-0.016	33.89	236	0.0106
3	±0.9623	0.8767	-0.299	0.301	0.048	-0.046	9.30	599	0.0046
4	±0.8137	0.9080	-0.251	0.252	0.041	-0.042	10.34	483	0.0063

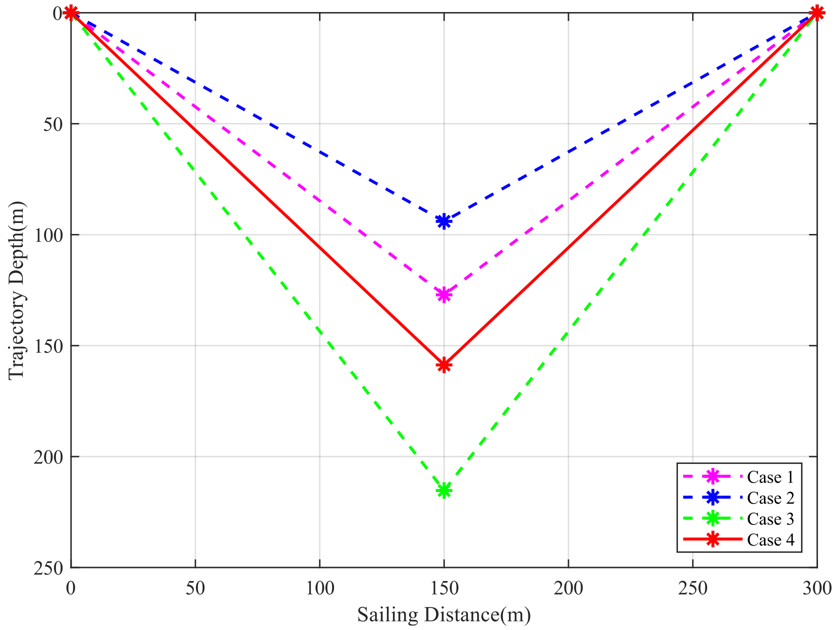

Fig. 9 Optimized gliding path for a single profile

We conducted a further study and analysis of the Pareto front derived from the NSGA-III optimization calculation, which consists of 100 nondominated solutions. From this array of nondominated solutions, four were selected, each exemplifying optimal and median evaluations across the three objective functions. For these four cohorts of nondominated solutions, the respective values of path parameters and control parameters for each solution are enumerated in Table 6. Figure 9 displays the results of the four selected numerical calculations.

When the rapid completion of exploration tasks is prioritized, the initial planning scheme outlined in the table is recommended; conversely, to optimize the quantity of detection tasks accomplished by the vehicle (thus minimizing energy consumption per profile movement), the second strategy should be employed; for objectives emphasizing the robot's detection range, the third plan is advisable. This paper advocates for the fourth solution delineated in the table, as it integrates multiple objectives including movement speed, vehicle energy consumption, and detection range, culminating in a more integrated and holistic performance.

5.1.2 Current conditions

The downstream state is taken as an example. In the numerical simulation, calculations are performed based on the working conditions: the target point is 300 m away. We assume a fixed ocean current speed of $v_{cx} = 0.15$ m/s.

In this context, the energy consumption indicator $E(V_1, \tau_1)$ in Equation (68) must be calculated according to the ocean conditions. The motion parameters in Equations (50), (53), and (54) are replaced with those in Equations (55), and (56) under ocean current conditions, and $\mathrm{x_{rd1}}$, $\mathrm{m_{rd1}}$ is calculated. After recalculating all the evaluation function indicators, based on the previous calculation results, we directly apply the multi-objective optimization algorithm based on the NSGA-III to solve this problem. Below are the path planning calculation results under ocean current conditions.

Table 7 The non-dominated solution computation results in ocean current environment.

Case	Angle (rad)	Velocity (m/s)	m_{bd1} (kg)	m_{bd2} (kg)	x_{rd1} (m)	x_{rd2} (m)	Energy (kJ)	Time (s)	Area (1/m)
1	±0.6001	0.3624	-0.102	0.104	0.035	-0.031	3.91	1003	0.0089
2	±0.4812	1.3814	-0.787	0.789	0.022	-0.024	27.23	245	0.0126
3	±1.0781	0.8536	-0.217	0.220	0.047	-0.045	8.95	743	0.0034
4	±0.7781	1.0583	-0.681	0.684	0.044	-0.042	11.23	398	0.0076

Similar to the condition without ocean currents, we employed NSGA-III to solve this multi-objective optimization problem through three independent computations. The results shown in Figure 10 indicate that the optimization is convergent. Additionally, the Pareto front depicted in the figure highlights the significant conflicts among the three objective functions under the ocean current condition. This Pareto front is also composed of 100 non-dominated solutions. From these, four solutions were selected, representing the optimal and median evaluations of the three objective functions. The path parameters and control parameters corresponding to each solution are listed in Table 7. Figure 11 visualizes the results of these four selected numerical calculations.

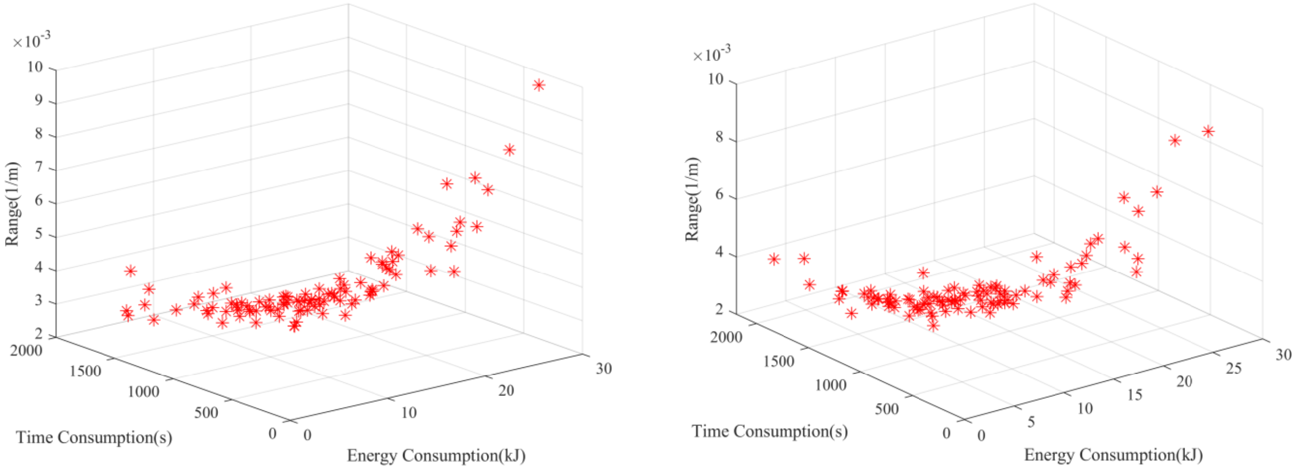

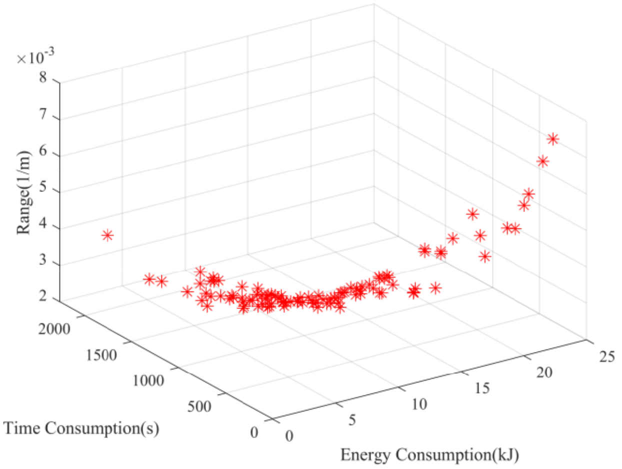

Fig. 10 Multi-objective optimization resulting in Pareto frontier in an ocean current environment

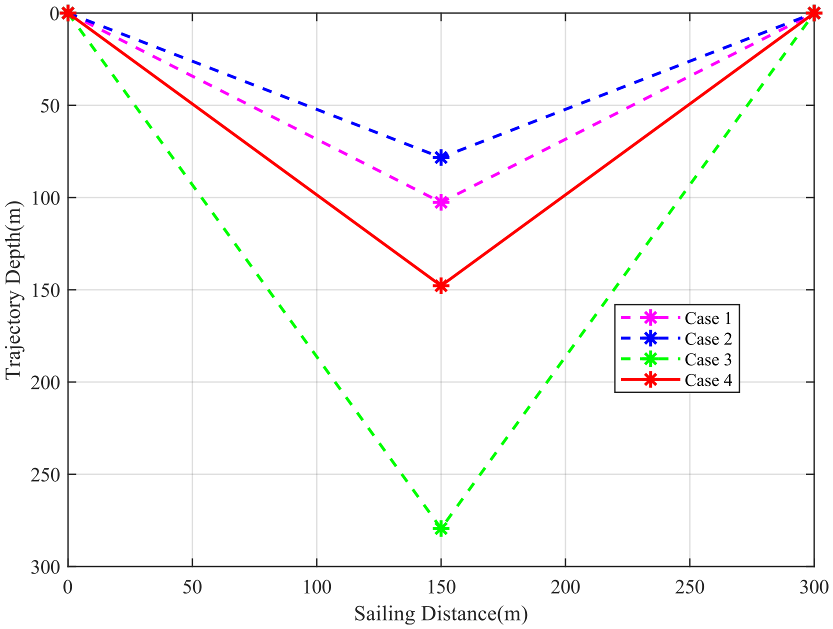

Fig. 11 Optimized single-profile gliding path in ocean current environment

Equation (56) demonstrates that the presence of a following current increases the relative angle of the vehicle in the fluid frame, thereby resulting in an augmented movement distance of the movable mass. Concurrently, there is a decrease in the relative speed between the vehicle and the fluid, consequently narrowing the adjustment spectrum of the buoyancy control device. Owing to the more pronounced impact of the buoyancy control device compared with the movement of the movable mass in the vehicle's energy consumption model, the aggregate energy expenditure under following the current conditions is diminished relative to that under still water conditions, which is corroborated by the numerical optimization results. The numerical simulation outcomes of three strategically selected path planning schemes under ocean current conditions are delineated in Figure 11.

5.2 Evaluation model for long-distance motion

The second detection mode involves long-distance multi-profile movement. In contrast with short-distance gliding strategies within a detection ambit, the spatial separation between two points in this mode is frequently substantial. To maintain the navigation depth within prescribed limits, it is often necessary to execute multiple dives and ascents. For the simplification of control dynamics during long-distance multi-profile gliding, consistent motion within each individual profile is ensured, and the descending and ascending phases of each profile are maintained in symmetry.

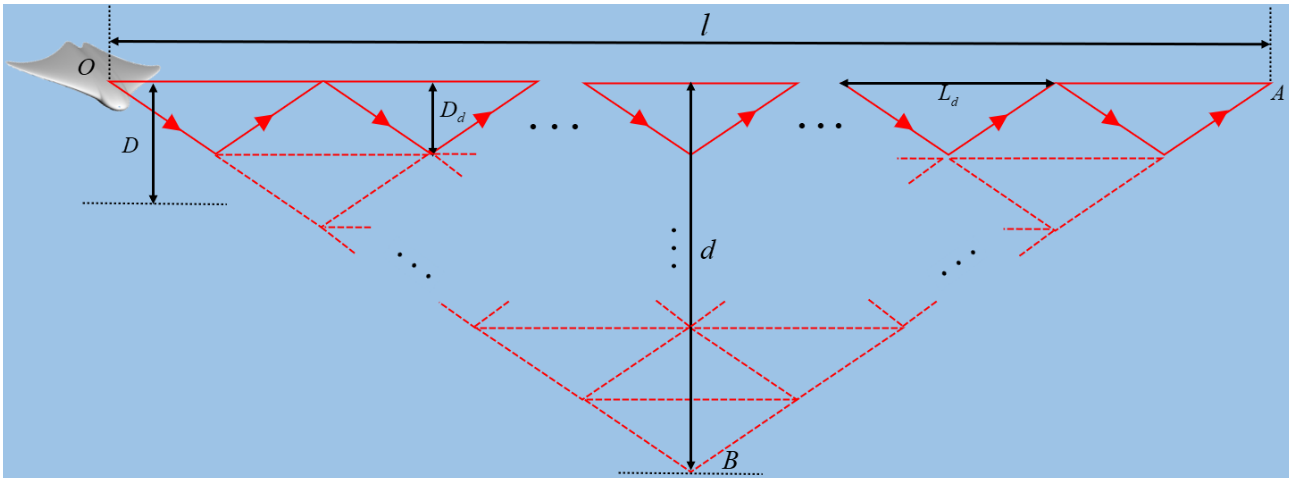

Fig. 12 Schematic of long-range multi-profile detection motion strategy

In the delineated gliding scenario, the entire trajectory consists of a series of single-profile cycles. As illustrated in Figure 12**,** we assume that the entire motion process is formed by concatenating identical isosceles triangles, where each base of the triangle represents the distance L_d that the vehicle moves in the X_e direction during a single profile motion. The desired depth for each profile motion remains consistent, denoted as D_d.

5.2.1 Without current conditions

As shown in Figure 12, we can translate the line segments of the motion path between points O and A, ultimately forming a large isosceles triangle OBA. Based on geometric knowledge, the following conclusion can be drawn: the actual gliding distance of multiple profiles is equivalent to the distance of an isosceles triangle with the line connecting the initial and end points (OA) as the base, and the target path parameter τ_d chosen during the planning process is the base angle. The gliding speed is determined by the selected target path parameter V_d. With the above conclusion in mind, when considering the time consumption under this scenario, its value is equal to the total time of individual profile movements. The time consumption function for this scenario can be expressed as follows:

$$T = \frac{nL}{V_d \cos(\tau_d)} \tag{72}$$

Similarly, the energy consumption function for this scenario can be expressed as the sum of the energy consumption for n identical cycles.

$$E = n(E_1 + E_2 + E_3 + E_4)/1000 \tag{73}$$

The detection range function depends on the target height D_d of the path planning, and simultaneously, the number of cycles in the above time and energy consumption functions also have a direct relationship with the depth of the path. As shown in Figure 12, the overall depth of the hypothetical path (OBA) formed after path translation is d. Equation (70) shows that the value of n in multi-profile gliding is directly proportional to the time and energy consumption. Therefore, under the constraint of target depth, it is essential to ensure that the value of n for each set of planned path parameters is minimized. Thus, we determine the value of n in the following manner.

$$n = \left\lceil \frac{d}{D} \right\rceil \tag{74}$$

where $d = nD_d = \frac{l}{2}|\tan\tau_d|$. By using the ceiling function to ensure the constraint $D_d \le D$, a smaller number of profiles n can be obtained when different path parameters are selected during the optimization calculation.

Since it is a detection task in a known environment, in this scenario, we disregard the detection area as an objective function in planning. Naturally, additional objective functions can be incorporated to accommodate evolving requirements for path configuration. By resolving the time and energy consumption functions pertinent to this scenario and ascertaining the optimal number of profiles, the subsequent mathematical model can be rigorously optimized,

$$\begin{cases} \min E\,(V_1,\tau_1), \min T\,(V_1,\tau_1) \\ s.t. \quad V_1 \in [V_{\max}, V_{\max}],\ \tau_1 \in \left(-\frac{\pi}{2}, -\tau_{\min}\right) \cup \left(\tau_{\min}, \frac{\pi}{2}\right) \\ \qquad\quad x_{rd1}, x_{rd2} \in [-0.05, 0.05], m_{bd1}, m_{bd2} \in [-1,1] \end{cases} \tag{75}$$

Calculations were performed under specified operational conditions: a target distance of 5000 m, a maximum depth constraint of 300 m, and quiescent water conditions. Consistent with the aforementioned research methodology, we used the NSGA-III algorithm to solve this optimization problem. However, under this condition, only two objective functions were considered: energy consumption and time expenditure. Through three independent NSGA-III computations, we obtained the Pareto front results shown in Figure 13, confirming the convergence of the optimization calculation. Moreover, the NSGA-III algorithm demonstrated excellent computational efficiency and cost-effectiveness, indicating its suitability for complex, long-distance, multi-profile path planning scenarios. The Pareto front in Figure 13 also illustrates the conflicting relationship between energy consumption and time expenditure during long-distance, multi-profile movements.

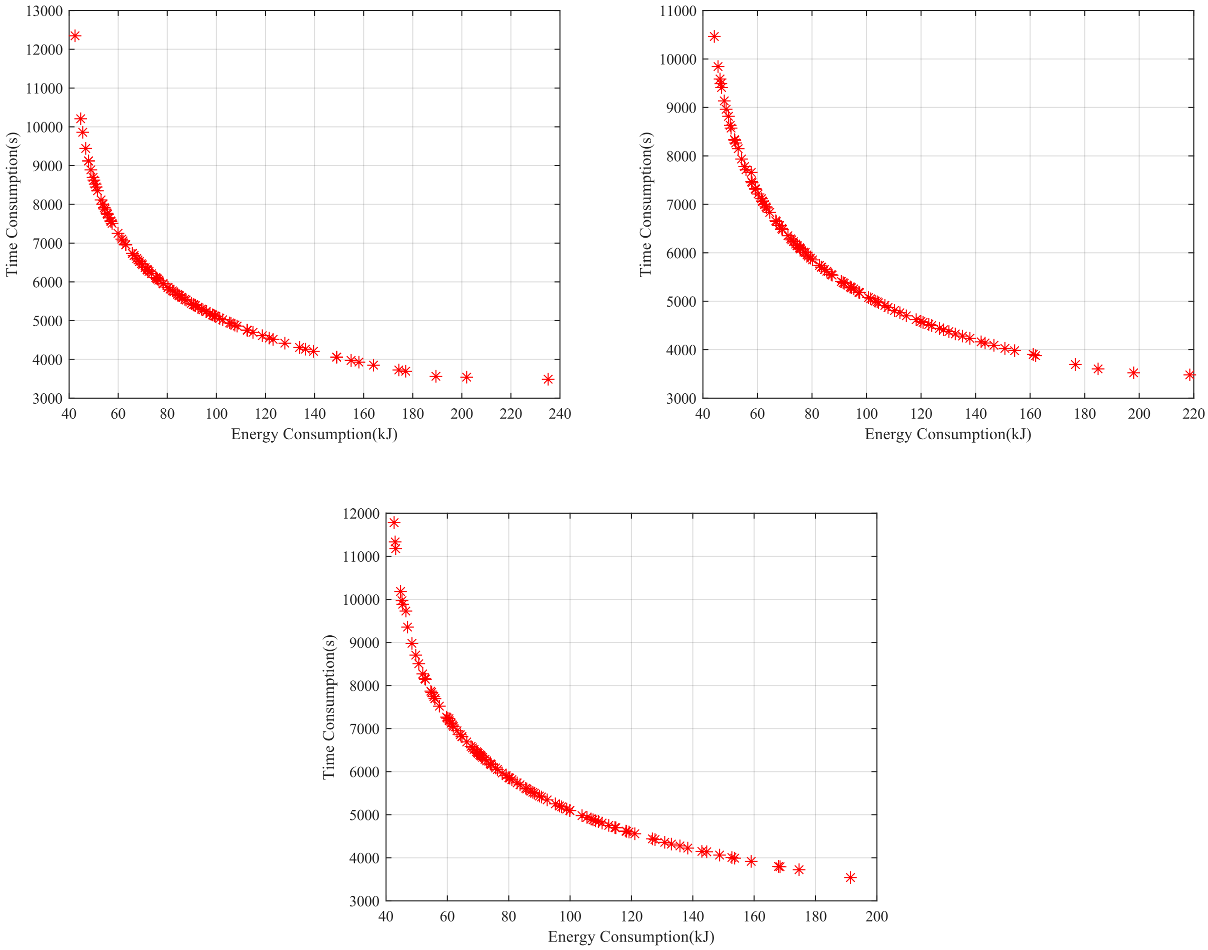

Fig. 13 Bi-objective optimization resulting in Pareto frontier

Table 8 NSGA-III multi-objective optimization computation parameters.

Population size	Number of generations	Crossover probability	Crossover index	Mutation probability	Mutation index
150	100	0.5	100	0.6	120

The table records the configuration parameters of the NSGA III algorithm used in solving this problem.

Table 9 The non-dominated solution computation results.

Case	Angle (rad)	Velocity (m/s)	m_{bd1} (kg)	m_{bd2} (kg)	x_{rd1} (m)	x_{rd2} (m)	Energy (KJ)	Time (s)	n
1	±0.4423	0.4003	-0.8511	0.8532	0.0152	-0.0139	44.1125	13821	4
2	±0.6315	1.4089	-0.1403	0.1421	0.033	-0.031	216.53	4397	7
3	±0.5277	0.9936	-0.4334	0.4352	0.0257	-0.0235	101.03	5824.5	5

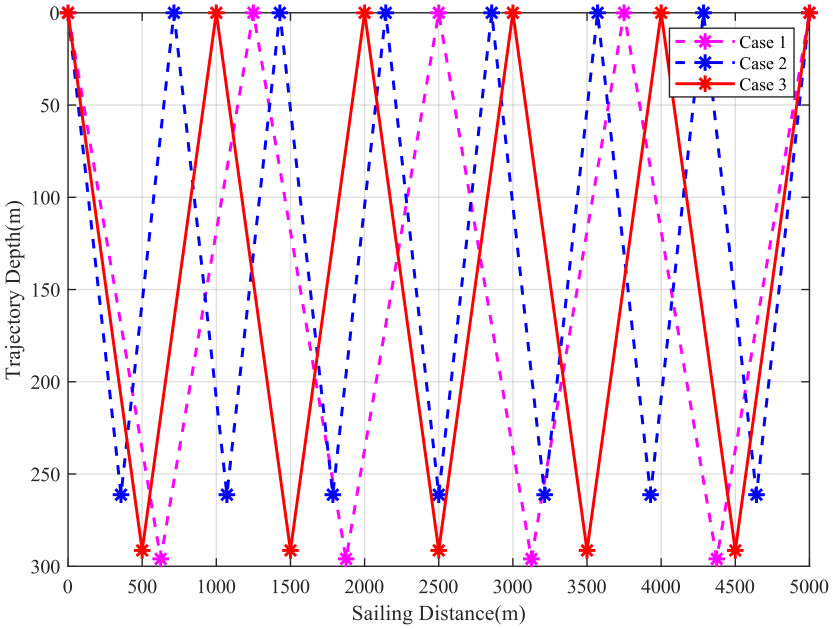

Fig. 14 Optimized gliding path for multiple profiles

The study and analysis are undertaken on the Pareto front, emanating from the NSGA-III optimization calculation, encompassing 150 nondominated solutions. Among these nondominated solutions, three were selected, each exemplifying the optimal criteria: one with the lowest energy consumption function, another with the minimum time function, and the third with median values for both objective functions. The values of the assorted path and control parameters corresponding to these three nondominant solutions are delineated in Table 9, while Figure 14 shows the outcomes of the three selected numerical calculations.

If the goal is to enable the glider to complete exploration tasks more quickly, the first planning scheme in the table can be adopted. When the vehicle aims to complete more exploration tasks, i.e., the lowest energy consumption, the second plan in the table should be used. In general, we recommend selecting the third solution from the table, as it takes into account both movement speed and energy consumption, offering a more comprehensive performance. This approach ensures a balanced consideration of both objectives, leading to a more holistic performance. The calculation results clearly show that the value of n is positively correlated with energy consumption, which verifies our derivation.

5.2.2 Current conditions

In the simulation, calculations are based on the working conditions: the target point is 5000 m away with a depth limit of 300 m. We selected the countercurrent environment, where $v_{cx} = -0.1$ m/s.

The energy consumption indicator $\mathrm{E}(\mathrm{V}_1, \tau_1)$ in Equation (68) must be calculated according to the ocean conditions. The motion parameters in Equations (50), (53), and (54) are replaced with those in Equations (57), and (58) under ocean current conditions, and x_{rd1}, m_{rd1} is calculated. We use the multi-objective optimization algorithm based on NSGA-III to plan the motion parameters under these conditions. The calculated results are presented in Table 10.

Table 10 The non-dominated solution computation results in ocean current environment.

Case	Angle (rad)	Velocity (m/s)	m_{bd1} (kg)	m_{bd2} (kg)	x_{rd1} (m)	x_{rd2} (m)	Energy (KJ)	Time (s)	n
1	±0.4437	0.4517	-0.197	0.216	0.0102	-0.0085	56.90	11848	4
2	±0.6083	1.4432	-0.928	0.925	0.0235	-0.0214	285.19	4254.9	6
3	±0.5314	1.2261	-0.7019	0.7191	0.0132	-0.0149	174.73	4628.8	5

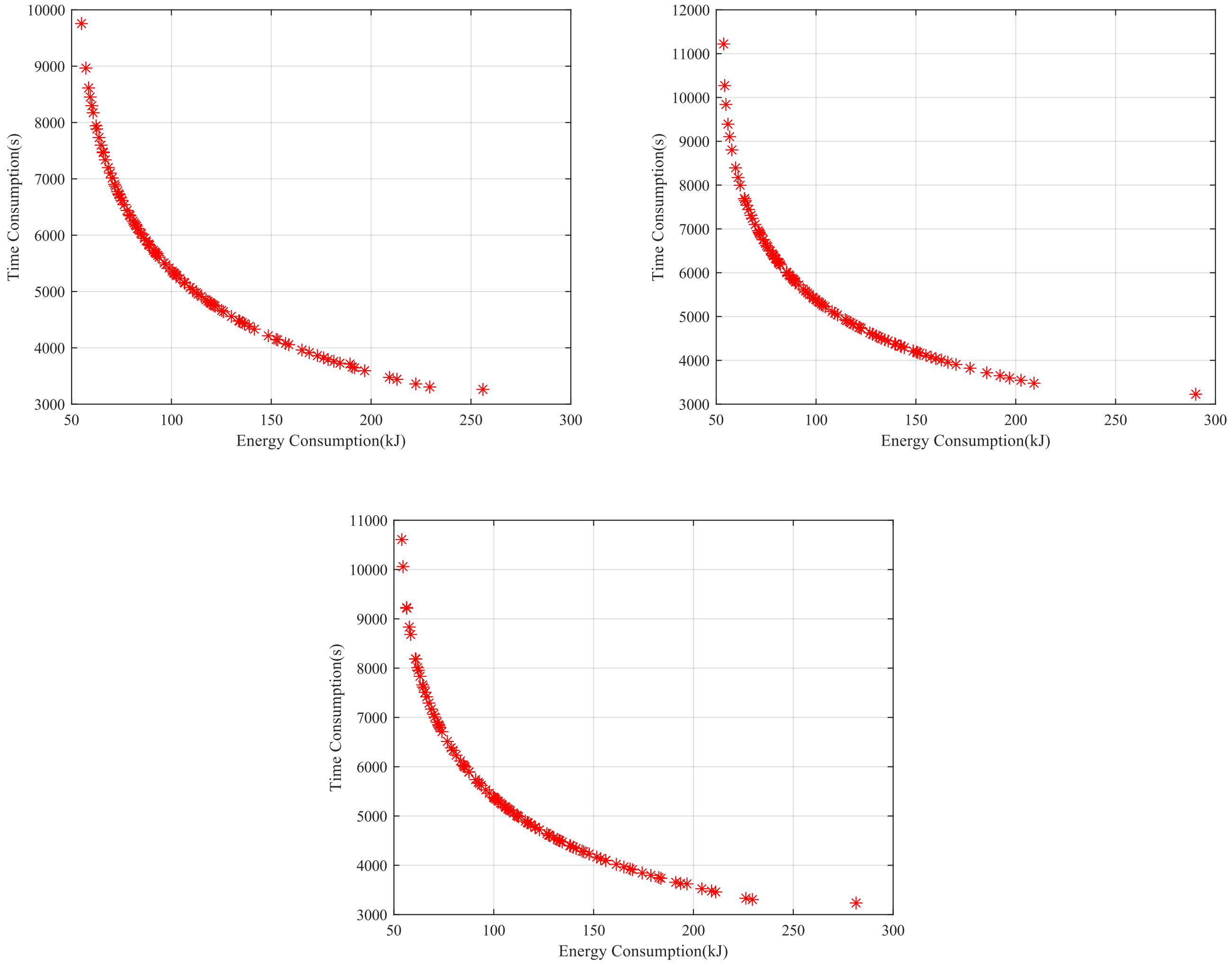

Fig. 15 Bi-objective optimization resulting in Pareto frontier in an ocean current environment

Figure 15 illustrates the Pareto frontiers derived from the trio of computational analyses. Figure 16 presents the triad of strategically planned paths, each numerically optimized for countercurrent conditions.

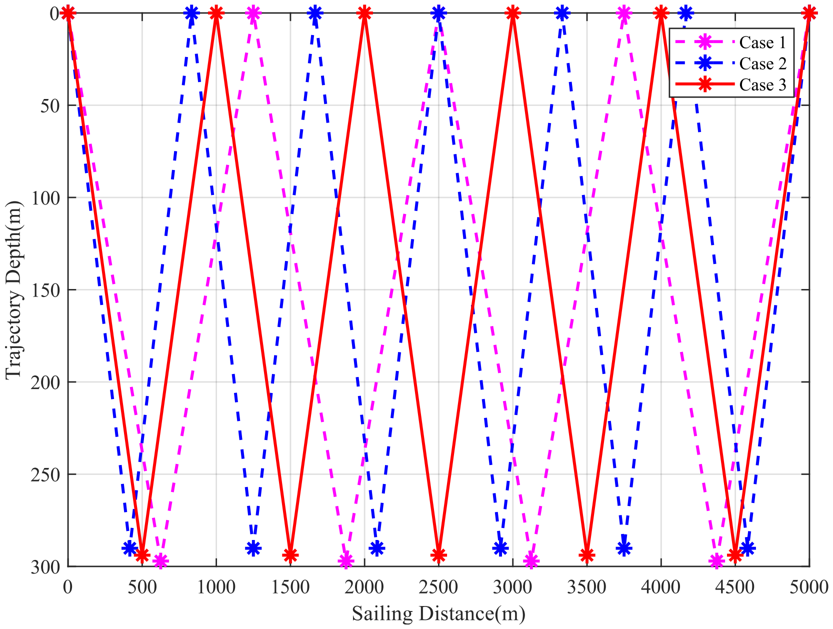

Fig. 16 Optimized multi-profile gliding path in ocean current environment

In the scenario of countercurrent conditions, the vehicle exhibits an increased relative motion speed with respect to the fluid, accompanied by a reduced motion angle, a phenomenon that is encapsulated in the formulated equations. Furthermore, the results from numerical simulations indicate that countercurrent conditions markedly augment the total energy expenditure of the underwater vehicle.

6. Conclusion

In this paper, a detailed study on the dynamic modelling of the gliding mode and path planning under ocean current conditions for a manta ray-inspired underwater vehicle is presented. The comprehensive system motion control model is formulated, incorporating the driving acceleration of the movable mass and the rate of change in the net buoyancy adjustment as control inputs. The proposed state-space model can improve the control accuracy. The focus on acceleration control enables a more refined management of the system's dynamics, which is particularly vital in scenarios demanding rapid response. Moreover, this methodology affords a more precise portrayal of the system's motion status, leading to augmented dynamic control capabilities, and yields an intuitive, readily analysable, and implementable mathematical model for future research endeavours. Subsequently, leveraging the aforementioned dynamic model, the study of the steady-state motion within a two-dimensional plane is conducted. The influence of ocean currents on a vehicle's steady-state gliding motion is meticulously analysed. The analysis results indicate that, under downcurrent conditions, the ocean current diminishes the vehicle's relative speed to the fluid and augments the relative angle, whereas under countercurrent conditions, it escalates the relative speed and reduces the relative angle.

The system model established in this study, which takes the adjustment rates of the controllers as control inputs, enables a more accurate description of the system's dynamic response. Compared to traditional methods that directly calculate system states based on the position of the sliding mass, our approach employs momentum conservation to establish the real-time interaction between the moving mass and the body. This renders the entire control process more representative of actual physical scenarios. The developed model provides an intuitive, analytically tractable, and easily implementable mathematical framework for future research.

Then, performance evaluation indicators for underwater gliding motion are developed through the derivation of dynamic equations. The motion process is characterized through the evaluation of energy consumption, time consumption, and detection range parameters. The analytical calculations reveal inherent contradictions among the various evaluation functions. Ultimately, comprehensive motion strategies are formulated, culminating in the establishment of a path planning process tailored for the vehicle gliding mode.

By integrating an evaluation model, the planning challenge is transformed into a multi-objective optimization problem, adeptly addressed using an NSGA-III based multi-objective optimization algorithm.

The numerical simulation results indicate that for single-profile gliding path planning, the proposed method reveals the conflicting relationships among the three performance indicators. Furthermore, based on the optimization algorithm's calculations, we can derive path planning solutions that satisfy different requirements. Similarly, in multi-profile motion planning, the Pareto front intuitively demonstrates the trade-off relationship between energy consumption and time consumption. Our path planning algorithm effectively identifies paths that balance these conflicting objectives, providing options for selection. This validates the effectiveness of the proposed path planning framework, which is capable of rapidly generating paths tailored to different objectives under both ocean current and non-current conditions. Additionally, the computational results further confirm the accuracy of the steady-state analysis in ocean current environments. Moreover, in multi-profile motion, the number of profiles n has the most significant impact on energy consumption, with higher profile numbers leading to greater energy consumption.

This study delves into the dynamic mechanisms underlying the impact of ocean currents on the gliding mode of a manta ray-inspired underwater vehicle, culminating in the establishment of steady-state gliding equations. Furthermore, it proposes a path optimization process for the vehicle, offering substantial theoretical guidance for analogous underwater vehicles.

This paper provides a relatively comprehensive theoretical research framework. However, there remains significant work to be carried out. Our future efforts will focus on conducting motion control research based on the dynamic system control model proposed in this study, to address the challenges posed by complex ocean environments. Additionally, we will validate the proposed research methods through underwater experiments using our engineering prototype, further refining the path planning research for underwater gliders.

ACKNOWLEDGMENT

This paper is Funded by the National Key Research and Development Program (2022YFC2805200).

NOMENCLATURE

$B = (m_h + m_b + m_r - m)g$	the net buoyancy of the vehicle
D	the width of the body
$(\boldsymbol{F_f} \quad \boldsymbol{T_f})^T$	$\boldsymbol{F_f} = (F_{fx} \quad F_{fy} \quad F_{fz})^T, \boldsymbol{T_f} = (T_{fx} \quad T_{fy} \quad T_{fz})^T$ the hydrodynamic forces and torques on the body in the flow frame
$(\boldsymbol{F_b} \quad \boldsymbol{T_b})^T$	$\boldsymbol{F_b} = (X_b \quad Y_b \quad Z_b)^T, \boldsymbol{T_f} = (K_f \quad M_f \quad N_f)^T$, the hydrodynamic forces and torques on the body in the body frame
$(\boldsymbol{F_e} \quad \boldsymbol{T_e})^T$	$\boldsymbol{F_e} = (X_e \quad Y_e \quad Z_e)^T, \boldsymbol{T_e} = (K_e \quad M_e \quad N_e)^T$ the hydrodynamic forces and torques on the body in the inertial frame
$\boldsymbol{I_a}$	added inertia tensor matrix of the body
$\boldsymbol{I_s}$	inertia tensor matrix of the static mass in the body frame
$\boldsymbol{I_r}$	inertia tensor matrix of the movable block in the frame of movable block
L	the length of the body
$\boldsymbol{M_a}$	added mass matrix of the body
$\boldsymbol{M_s}$	mass matrix of the static mass
$\boldsymbol{M_n}, \boldsymbol{I_n}$	the generalized system mass matrix and the generalized system inertia tensor matrix

m, m_s, m_b, m_r, m_h $m_s = m_h + m_b$	the vehicle displacement mass, the static mass, the mass of the adjustable net buoyancy, the mass of the movable block, and the mass of the static hull
$\boldsymbol{N} = (\boldsymbol{V} \quad \boldsymbol{W})^T$	$\boldsymbol{V} = (x \quad y \quad z)^T$ the position of the body in the inertial frame, $\boldsymbol{W} = (\phi \quad \theta \quad \varphi)^T$ the attitude of the body in the inertial frame
$\boldsymbol{n} = (\boldsymbol{v} \quad \boldsymbol{w})^T$	$\boldsymbol{v} = (v_1 \quad v_2 \quad v_3)^T$ the linear velocity of the body in the body frame, $\boldsymbol{w} = (w_1 \quad w_2 \quad w_3)^T$ the angular velocity of the body in the body frame
$O_e(X_e, Y_e, Z_e)$	the inertial frame
$O_b(X_b, Y_b, Z_b)$	the body frame
$O_r(X_r, Y_r, Z_r)$	the local frame of movable block
$O_f(X_f, Y_f, Z_f)$	the flow frame
$\boldsymbol{P_{rb}} = (P_{rbx} \quad P_{rby} \quad P_{rbz})^T$, $\boldsymbol{L_{rb}} = (L_{rbx} \quad L_{rby} \quad L_{rbz})^T$	linear momentum and angular momentum of the movable block in the body frame
$\boldsymbol{P_r} = (P_{rx} \quad P_{ry} \quad P_{rz})^T$, $\boldsymbol{L_r} = (L_{rx} \quad L_{ry} \quad L_{rz})^T$	linear momentum and angular momentum of the movable block in the frame of movable block
$\boldsymbol{R_1}$	rotation matrix linear velocity from the body frame to the inertial frame
$\boldsymbol{R_2}$	rotation matrix angular velocity from the body frame to the inertial frame
$\boldsymbol{R_3}$	rotation matrix from the movable block frame to the body frame
$\boldsymbol{R_4}$	rotation matrix from the flow frame to the body frame
$\boldsymbol{R_s} = (x_s \quad y_s \quad z_s)^T$, $\boldsymbol{R_b} = (x_b \quad y_b \quad z_b)^T$, $\boldsymbol{R_r} = (x_r \quad y_r \quad z_r)^T$, $\boldsymbol{R_h} = (x_h \quad y_h \quad z_h)^T$	coordinates of the center of mass for the static mass, the buoyancy adjustment device, the movable block, and the static hull in the body frame
r	distance from the center of mass of the movable block to the X-axis in the body frame
$\boldsymbol{V_c}, \boldsymbol{v_c}$	ocean current velocity in the inertial frame and the body frame
$\boldsymbol{v_r} = (v_{rx} \quad v_{ry} \quad v_{rz})^T$	relative velocity of the movable mass in the body frame
$\boldsymbol{w_r} = (w_{rx} \quad w_{ry} \quad w_{rz})^T$	relative angular velocity of the movable mass in the body frame
α	the attack angle
β	the slip angle
$\boldsymbol{\eta_e} = (\boldsymbol{P_e} \quad \boldsymbol{L_e})^T$	$\boldsymbol{P_e}$ linear momentum of the static mass in the inertial frame, $\boldsymbol{L_e}$ angular momentum of the static mass in the inertial frame
$\boldsymbol{\eta_b} = (\boldsymbol{P_b} \quad \boldsymbol{L_b})^T$	$\boldsymbol{P_b}$ linear momentum of the static mass in the body frame, $\boldsymbol{L_b}$ angular momentum of the static mass in the body frame
λ	rotation angle of the movable mass about the X-axis in the body frame

REFERENCES

[1] Yang, L., 2024. Small Modular AUV Based on 3D Printing Technology: Design, Implementation and Experimental Validation. *Brodogradnja*. 75(1), 75104. https://doi.org/10.21278/brod75104

[2] Hou, S., Zhang, Z., Lian, H., Xing, X., Gong, H., Xu, X., 2022. Hull shape optimization of small underwater vehicle based on Kriging-based response surface method and multi-objective optimization algorithm. *Brodogradnja*, 73(3), 111-134. https://doi.org/10.21278/brod73307

[3] Jiang, C.; Tang, Y.; Wang, J.; Zhang, W.; Zhou, M.; Niu, J.; Wan, L.; Chen, G.; Wu, G.; Cheng, X. 2024, An optimized method for AUV trajectory model in benthonic hydrothermal area based on improved slime mold algorithm. Brodogradnja 75, 1-25. https://doi.org/10.21278/brod75401

[4] Liu, J.; Yue, Q.; Wu, S.; Yue, X. 2024, Hydrodynamic shape optimization of an autonomous and remotely-operated vehicle via a multi-surrogate model. Brodogradnja 75, 1-19. https://doi.org/10.21278/brod75301

[5] Wang, Z., Wei, Z., Yu, C., Cao, J., Yao, B., Lian, L., 2023. Dynamic modeling and optimal control of a positive buoyancy diving autonomous vehicle. *Brodogradnja*. 74(1), 19-40. https://doi.org/10.21278/brod74102

[6] Eriksen, C. C., Osse, T. J., Light, R. D., Wen, T., Lehman, T. W., Sabin, P. L., Ballard, J. W., Chiodi, A. M., 2001. Seaglider: a long-range autonomous underwater vehicle for oceanographic research. *IEEE Journal of Oceanic Engineering*, 26, 424-436. https://doi.org/10.1109/48.972073

[7] Sherman, J., Davis, R.E., Owens, W. B., Valdes, J., 2001. The autonomous underwater glider "Spray". *IEEE Journal of Oceanic Engineering*, 26, 437-446. https://doi.org/10.1109/48.972076

[8] Wang, S., 2014. Dynamic Modeling of Hybrid Underwater Glider Based on the Theory of Differential Geometry and Sea Trails. *Journal of Mechanical Engineering*, 50, 19. https://doi.org/10.3901/JME.2014.02.019

[9] Webb, D. C., Simonetti, P. J., Jones, C. P., 2001. SLOCUM: an underwater glider propelled by environmental energy. *IEEE Journal of Oceanic Engineering*, 26, 447-452. https://doi.org/10.1109/48.972077

[10] Petritoli, E., Leccese, F., 2018. High Accuracy Attitude and Navigation System for an Autonomous Underwater Vehicle (AUV). *ACTA IMEKO*, 7, 3. https://doi.org/10.21014/acta_imeko.v7i2.535

[11] Zhou, H., Wang, T., Sun, L., Lan, W., 2020. Study on the vertical motion characteristics of disc-type underwater gliders with zero pitch angle. *Journal of Marine Science and Technology*, 25, 828-841. https://doi.org/10.1007/s00773-019-00683-8

[12] Xie, X., Wang, Y., Song, Y., Yang, S., Luo, C., Ma, W., Lian, Y., 2021. Development, optimization, and evaluation of a hybrid passive buoyancy compensation system for underwater gliders. *Ocean Engineering*, 242, 110115. https://doi.org/10.1016/j.oceaneng.2021.110115

[13] Yang, Y., Liu, Y., Wang, Y., Zhang, H., Zhang, L., 2017. Dynamic modeling and motion control strategy for deep-sea hybrid-driven underwater gliders considering hull deformation and seawater density variation. *Ocean Engineering*, 143, 66-78. https://doi.org/10.1016/j.oceaneng.2017.07.047

[14] Wang, B., Xiong, J., Wang, S., Ma, D., Liu, C., 2022. Steady motion of underwater gliders and stability analysis. *Nonlinear Dynamics*, 107, 515-531. https://doi.org/10.1007/s11071-021-07045-3

[15] Jing, G., Lei, L., Gang, Y., 2022. Dynamic modeling and experimental analysis of an underwater glider in the ocean. *Applied Mathematical Modelling*, 108, 392-407. https://doi.org/10.1016/j.apm.2022.03.034

[16] Leonard, N. E., Graver, J. G., 2001. Model-based feedback control of autonomous underwater gliders. IEEE Journal of *Oceanic Engineering*, 26, 633-645. https://doi.org/10.1109/48.972106

[17] Zhang, S., Yu, J., Zhang, A., Zhang, F., 2013. Spiraling motion of underwater gliders: Modeling, analysis, and experimental results. *Ocean Engineering*, 60, 1-13. https://doi.org/10.1016/j.oceaneng.2012.12.023

[18] Fan, S., Woolsey, C. A., 2014. Dynamics of underwater gliders in currents. *Ocean Engineering*, 84, 249-258. https://doi.org/10.1016/j.oceaneng.2014.03.024

[19] Zhao, B., Wang, X., Yao, B., Lian, L., 2015. Lyapunov stability analysis of the underwater glider. *Journal of Harbin Engineering University*, 36, 83-87.

[20] Liu, Y., Shen, Q., Ma, D., Yuan, X., 2016. Theoretical and experimental study of anti-helical motion for underwater glider. *Applied Ocean Research*, 60, 121-140. https://doi.org/10.1016/j.apor.2016.09.001

[21] Lyu, D., Song, B., Pan, G., Yuan, Z., Li, J., 2019. Winglet effect on hydrodynamic performance and trajectory of a blended-wing-body underwater glider. *Ocean Engineering*, 188, 106303. https://doi.org/10.1016/j.oceaneng.2019.106303

[22] Lei, L., Gang, Y., Jing, G., 2022. Physics-guided neural network for underwater glider flight modeling. *Applied Ocean Research*, 121, 103082. https://doi.org/10.1016/j.apor.2022.103082

[23] Wang, Y. H., Wang, S. X., 2009. Dynamic Modeling and Three-Dimensional Motion Analysis of Underwater Gliders. *China Ocean Engineering*, 23, 489-504.

[24] Mahmoudian, N., Geisbert, J., Woolsey, C., 2010. Approximate Analytical Turning Conditions for Underwater Gliders: Implications for Motion Control and Path Planning. *IEEE Journal of Oceanic Engineering*, 35, 131-143. https://doi.org/10.1109/JOE.2009.2039655

[25] Song, Y., Wang, Y., Yang, S., Wang, S., Yang, M., 2020. Sensitivity analysis and parameter optimization of energy consumption for underwater gliders. *Energy*, 191, 116506. https://doi.org/10.1016/j.energy.2019.116506

[26] Yu, J., Zhang, F., Zhang, A., Jin, W., Tian, Y., 2013. Motion Parameter Optimization and Sensor Scheduling for the Sea-Wing Underwater Glider. *IEEE Journal of Oceanic Engineering*, 38, 243-254. https://doi.org/10.1109/JOE.2012.2227551

[27] Zamuda, A., Sosa, J. D. H., 2019. Success history applied to expert system for underwater glider path planning using differential evolution. *Expert Systems with Applications*, 119, 155-170. https://doi.org/10.1016/j.eswa.2018.10.048

[28] Zamuda, A., Hernández Sosa, J. D., 2014. Differential evolution and underwater glider path planning applied to the short-term opportunistic sampling of dynamic mesoscale ocean structures. *Applied Soft Computing*, 24, 95-108. https://doi.org/10.1016/j.asoc.2014.06.048

[29] Zamuda, A., Hernández Sosa, J. D., Adler, L., 2016. Constrained differential evolution optimization for underwater glider path planning in sub-mesoscale eddy sampling. *Applied Soft Computing*, 42, 93-118. https://doi.org/10.1016/j.asoc.2016.01.038

[30] Yoon, S., Kim, J., 2018- Trajectory Design of Underwater Gliders for Maximum Advance Speed in Finite-Depth Water. *Journal of Guidance, Control, and Dynamics*, 41, 742-750. https://doi.org/10.2514/1.G002891

[31] Yang, M., Wang, Y., Wang, S., Yang, S., Song, Y., Zhang, L., 2019. Motion parameter optimization for gliding strategy analysis of underwater gliders. *Ocean Engineering*, 191, 106502. https://doi.org/10.1016/j.oceaneng.2019.106502

[32] Wang, S., Yang, M., Niu, W., Wang, Y., Yang, S., Zhang, L., Deng, J., 2021. Multidisciplinary design optimization of underwater glider for improving endurance. *Structural and Multidisciplinary Optimization*, 63, 2835-2851. https://doi.org/10.1007/s00158-021-02844-z

[33] Wu, H., Niu, W., Wang, S., Yan, S., 2021. An optimization method for control parameters of underwater gliders considering energy consumption and motion accuracy. *Applied Mathematical Modelling*, 90, 1099-1119. https://doi.org/10.1016/j.apm.2020.10.015

[34] Wu, H., Niu, W., Wang, S., Yan, S., 2021. Multi-objective optimization for control parameters of underwater gliders considering effect of uncertain input errors. *Proceedings of the Institution of Mechanical Engineers, Part C: Journal of Mechanical Engineering Science*, 236, 3093-3110. https://doi.org/10.1177/09544062211036481

[35] Cai, J., Zhang, F., Sun, S., Li, T., 2021. A meta-heuristic assisted underwater glider path planning method. *Ocean Engineering*, 242, 110121. https://doi.org/10.1016/j.oceaneng.2021.110121

[36] Wu, H., Niu, W., Zhang, Y., Wang, S., Yan, S., 2022. Multidisciplinary optimization-based path planning for underwater gliders executing multi-point exploration missions. *Ocean Engineering*, 266, 113022. https://doi.org/10.1016/j.oceaneng.2022.113022

[37] Lan, W., Jin, X., Chang, X., Wang, T., Zhou, H., Tian, W., Zhou, L., 2022. Path planning for underwater gliders in time-varying ocean current using deep reinforcement learning. *Ocean Engineering*, 262, 112226. https://doi.org/10.1016/j.oceaneng.2022.112226

[38] Wang, S., Yang, M., Wang, Y., Yang, S., Lan, S., Zhang, X., 2021. Optimization of Flight Parameters for Petrel-L Underwater Glider. *IEEE Journal of Oceanic Engineering*, 46, 817-828. https://doi.org/10.1109/JOE.2020.3030573

[39] Tian, X., Zhang, H., Zhou, H., Zhang, L., 2024. Synthesis optimization of underwater glider motion parameters based on the total energy consumption model. *Ocean Engineering*, 297, 117103. https://doi.org/10.1016/j.oceaneng.2024.117103

[40] Hu, H., Zhang, Z., Li, L., Peng, X., 2023. Energy-optimal motion planning of underwater gliders accounting for seabed topography and ocean currents. *Ocean Engineering*, 288, 116008. https://doi.org/10.1016/j.oceaneng.2023.116008

[41] Hu, H., Zhang, Z., Wang, T., Peng, X., 2024. Underwater glider 3D path planning with adaptive segments and optimal motion parameters based on improved JADE algorithm. *Ocean Engineering*, 299, 117377. https://doi.org/10.1016/j.oceaneng.2024.117377

[42] Sun, C., Song, B., Wang, P., 2015. Parametric geometric model and shape optimization of an underwater glider with blended-wing-body. *International Journal of Naval Architecture and Ocean Engineering*, 7, 995-1006. https://doi.org/10.1515/ijnaoe-2015-0069

[43] Jing, A., Wang, J., Gao, J., Chen, Y., Cao, Y., Cao, Y., Pan, G., 2022. Self-tuning adaptive active disturbance rejection pitch control of a manta-ray-like underwater glider. *Ocean Engineering*, 254, 111364. https://doi.org/10.1016/j.oceaneng.2022.111364

[44] Fossen, T., 2021. Handbook of Marine Craft Hydrodynamics and Motion Control. *John Wiley & Sons, Ltd*. https://doi.org/10.1002/9781119575016

[45] Graver, J. G., 2005. Underwater gliders: dynamics, control and design. *Doctoral dissertation*. Princeton University, New Jersey, USA.

[46] Wu, H., Niu, W., Wang, S., Yan, S., 2022. A feedback control strategy for improving the motion accuracy of underwater gliders in currents: Performance analysis and parameter optimization. *Ocean Engineering*, 252, 111250. https://doi.org/10.1016/j.oceaneng.2022.111250

[47] Fu, X., Lei, L., Yang, G., Li, B., 2018. Multi-objective shape optimization of autonomous underwater glider based on fast elitist non-dominated sorting genetic algorithm. *Ocean Engineering*, 157, 339-349. https://doi.org/10.1016/j.oceaneng.2018.03.055

APPENDIX

This section presents the Pareto frontiers obtained from multiple optimization computations conducted in this study. Specifically, Figures 17 and 18 illustrate the optimization results of a single profile under static water conditions using MOPSO and NSGA-III, respectively. Figure 19 depicts the optimization results of a single profile motion under downstream flow conditions using NSGA-III.

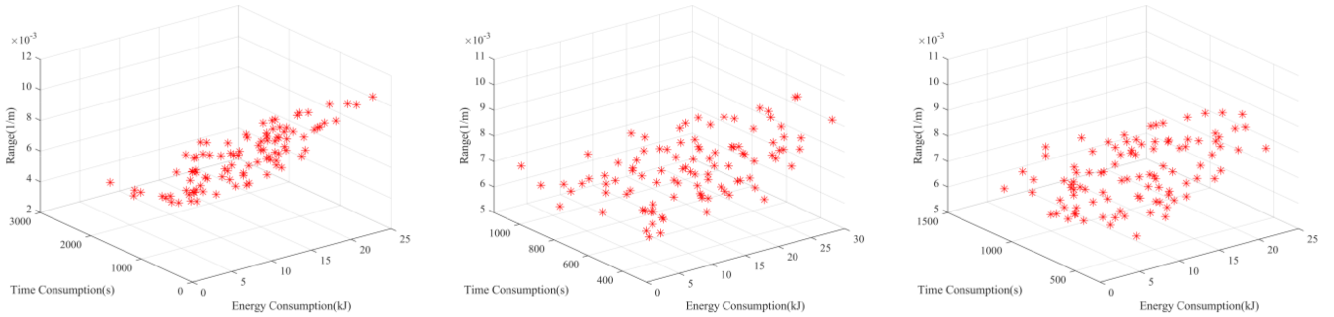

Fig. 17 Pareto frontier of multi-objective optimization for the single-profile using MOPSO.

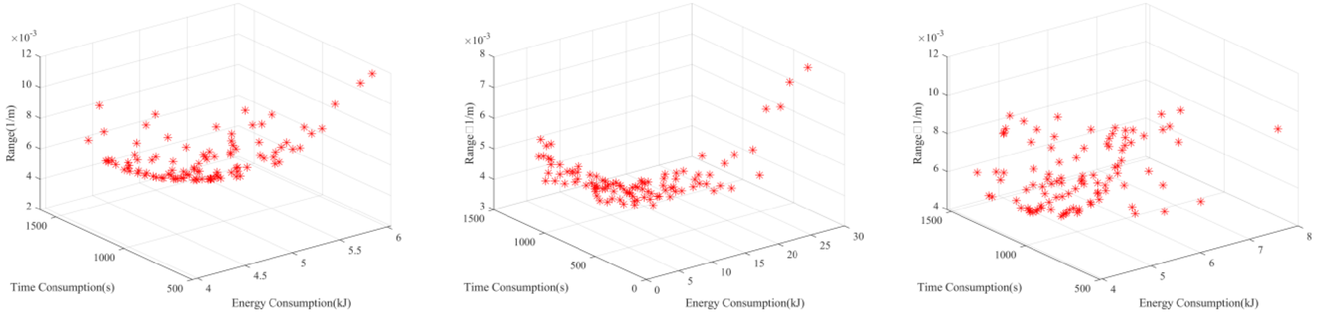

Fig. 18 Pareto frontier of multi-objective optimization for the single-profile using NSGA-III.

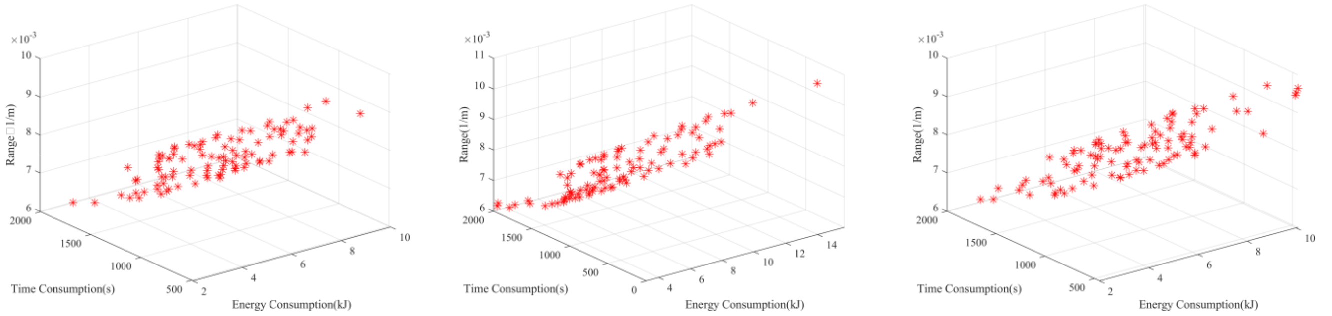

Fig. 19 Pareto frontier of multi-objective optimization for the single-profile in current conditions.

Figure 20 presents the optimization results of multiple profile motions under static water conditions using NSGA-III. Figure 21 illustrates the optimization results of multiple profile motions under counterflow conditions using NSGA-III.

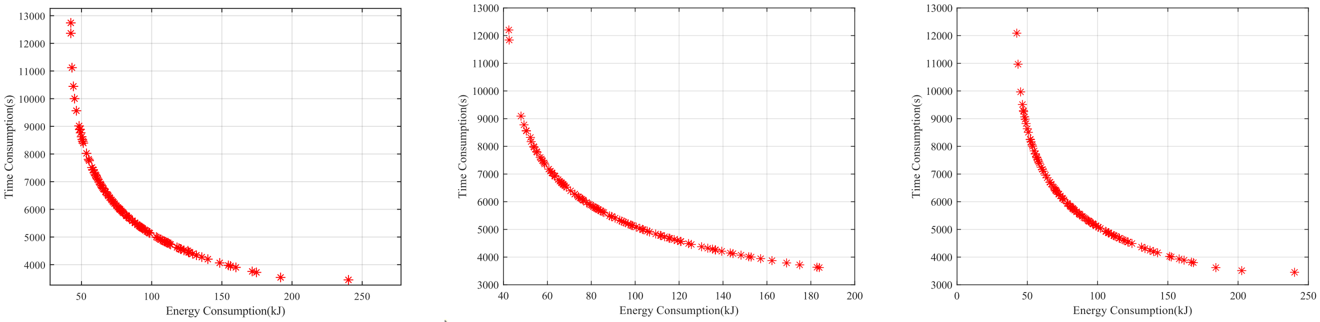

Fig. 20 Pareto frontier of multi-objective optimization for the long-range multi-profile.

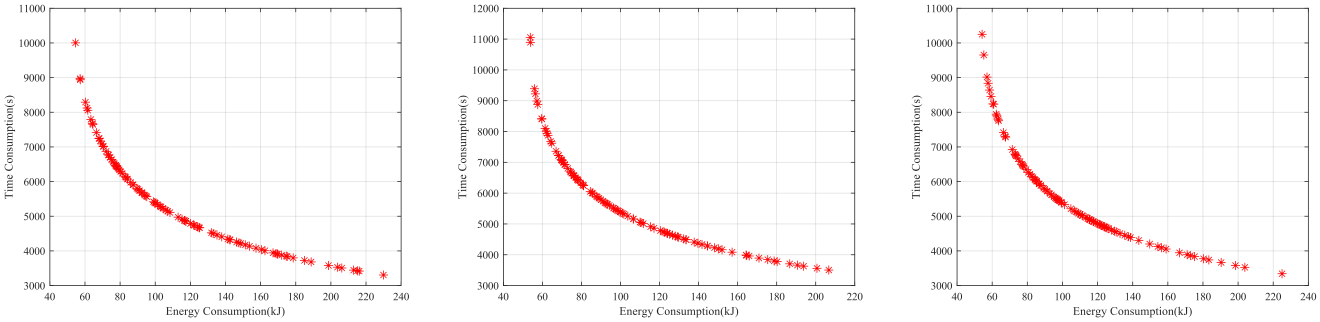

Fig. 21 Pareto frontier of multi-objective optimization for the long-range multi-profile in current conditions.